Quaternion-Based Attitude Control of a Solar Sail Using a Gimballed Mass and Tip Vanes

by

B. Nero

Supervisor: Professor C. Damaren

April 7, 2023

Abstract

Solar sailing is a spacecraft propulsion concept that harnesses solar radiation pressure to generate thrust. One caveat of solar sail spacecraft is that their large surface areas, and consequently large moments of inertia, render traditional spacecraft attitude control technologies ineffective. As a result, alternative methods must be implemented to achieve attitude control of a solar sail spacecraft. This thesis investigates the combination of two actuators proposed by existing research, a gimballed mass and tip vanes, to achieve three-axis attitude control of a solar sail.

This research was carried out in three phases. The first phase investigated the effectiveness of a control system using only a gimballed mass to achieve two-axis attitude control. It compared the results between two types of simulations: one that considers actuator dynamics and one that does not. The second phase added two single-degree-of-freedom tip vanes to the control system to achieve three-axis control, while also comparing the difference in results with and without actuator dynamics. The third phase investigated the sensitivity of the system response to changes in the natural frequency of the actuator motors, the gimballed payload mass, and the tip vane surface area. Second-order actuator dynamics have been incorporated into the system to better understand their effect on the system response.

Overall, the results indicate that a solar sail equipped with a gimballed mass and two single-degree-of-freedom tip vanes is capable achieving three-axis attitude control under a range of initial conditions. It was discovered that the effect of actuator dynamics becomes more significant at larger initial angular velocities, and that larger actuator motor natural frequencies are necessary to ensure the system converges. It was also discovered for some of the cases in Phase 3 that to achieve faster settling times, it is necessary to increase the tip vane surface area, however increasing the gimballed payload's mass did not have a significant affect on the results.

Acknowledgements

Firstly, I would like to thank my thesis supervisor, Professor Christopher Damaren, for his guidance and support throughout this project. I have gained a much a better understanding of spacecraft dynamics and control and I am incredibly grateful to have have worked under the tutelage of an expert in the field.

I would also like to thank my family for their support throughout my undergraduate program and for encouraging me to pursue opportunities for continued learning and growth.

Contents

List of Figures

List of Acronyms

AU - Astronomical Unit

IKAROS - Interplanetary Kite-craft Accelerated by Radiation Of the Sun

JAXA - Japan Aerospace Exploration Agency

JPL - Jet Propulsion Laboratory

NASA - National Aeronautics and Space Administration

NEA Scout - Near-Earth Asteroid Scout

ODE - Ordinary Differential Equation

PD - Proportional-Derivative

SDOF - Single Degree-of-Freedom

SRP - Solar Radiation Pressure

Variable Nomenclature

$\boldsymbol{F}$ - Solar radiation pressure force vector

P - Solar radiation pressure

A_s - Sail membrane surface area

A_{tv} - Tip vane surface area

$\hat{\boldsymbol{s}}_b$ - Unit Sun vector in the spacecraft body frame

$\hat{\boldsymbol{n}}$ - Sail anti-Sunward surface unit normal vector in the spacecraft body frame

γ - Sail thrust coefficient

$\boldsymbol{C}_{bo}$ - Rotation matrix from the orbital frame to the spacecraft body frame

$\boldsymbol{\epsilon}$ - Vector part of the quaternion

η - Scalar part of the quaternion

$\boldsymbol{I}$ - Moment of inertia matrix

$\boldsymbol{\omega}$ - Vector containing solar sail angular velocities

$T_{c,d}$ - Vector containing desired control torques

K_p - Proportional control gain

K_d - Derivative control gain

cm_s - Solar sail center of mass (excluding gimballed rod and payload)

cm_p - Gimballed payload center of mass

cm_r - Gimballed rod center of mass

cm_t - Total system center of mass

cp - Center of pressure

θ_g - Gimbal cone angle

ϕ_g - Gimbal clock angle

δ_1 - Tip vane 1 angle

δ_2 - Tip vane 2 angle

l - Length of gimballed rod

b - Height of gimbal mechanism

w - Tip vane width

h - Tip vane height

m_p - Gimballed payload mass

m_r - Gimballed rod mass

m_s - Sail subsystem mass (includes sail film, booms, central hub)

m_{tv} - Tip vane mass

m_t - Total system mass

T_{b_1} - Control torque about the b_1 axis

T_{b_2} - Control torque about the b_2 axis

T_{b_3} - Control torque about the b_3 axis

ζ - Damping ratio

ω_n - Natural frequency of motors driving the gimbal mechanism and tip vanes

t_s - Settling time

1 Introduction

Solar sailing is an innovative propulsion concept that utilizes large reflective membranes and momentum transfer from solar radiation as a means of propulsion. Unlike conventional propulsion methods, solar sails are not hindered by a finite propellant mass and are therefore capable of providing continuous acceleration, with the only limiting factor being degradation of the sail's optical properties. Solar sails also have high area-to-mass ratios, enabling them to achieve large accelerations over time. These characteristics make solar sailing a desirable means of long duration spaceflight missions, such as those intended for interplanetary, or even interstellar destinations.

1.1 A Brief History of Solar Sailing

Various studies on solar sails have been conducted throughout the 20th and 21st centuries. In 1958, Richard Garwin authored a paper on the feasibility of using commercially available aluminized plastic film as a means of space vehicle propulsion [1]. In the late 1970's, JPL engineers studied a mission concept for a rendezvous with Halley's comet using both square and heliogyro solar sail designs [2]. In the early-to-mid 2000's, ATK Space Systems and L'Garde, designed and built 20 m-span solar sails for NASA's In-Space Propulsion Technology Program [3]. Deployment and functional vacuum testing of these designs were successfully completed at NASA Glenn's Space Power Facility [3]. NASA continued work on solar sails, and in 2011, demonstrated autonomous sail deployment with their NanoSail-D2 spacecraft, which used a 3.5 $\times$ 3.5 m sail [4].

Up until 2010, deep space solar sailing had only been a theoretical concept, the feasibility of which had not been physically demonstrated. This changed in May 2010 when JAXA launched the IKAROS solar sail spacecraft on a mission to Venus, marking the first use of solar sails in deep space [5]. During the mission, IKAROS successfully deployed a 20 m-span solar sail, performed a Venus flyby, and measured the acceleration induced by solar radiation

pressure, demonstrating that solar radiation pressure could be used for accelerating a solar sail in interplanetary space [5].

Other in-space solar sailing demonstrations include The Planetary Society's LightSail missions: LightSail 1 and LightSail 2. Prior to these missions, the Planetary Society had previously attempted to launch a solar sail in 2005, however the first stage of its launch vehicle had failed, and the spacecraft was unable to achieve the desired orbital altitude [6]. The Planetary Society's next mission, the three-unit (3U) CubeSat-sized LightSail 1 spacecraft, successfully deployed in June 2015 and spent 25 days in low-Earth orbit before re-entering Earth's atmosphere [7]. The follow-up mission, LightSail 2, demonstrated an orbit raising maneuver by performing two 90-degree reorientations per orbit in July 2019 [8].

A more recent attempt at deep space solar sailing was NASA's NEA Scout spacecraft. Similar to the NanoSail-D2 and LightSail missions, NEA Scout also used a CubeSat-style design, but with a 6U form factor. The spacecraft launched alongside NASA's Artemis I mission with the objective of visiting the near-Earth Asteroid 2020 GE [9]. As of December 2022, contact with the spacecraft has yet to be established [10].

1.2 Solar Sail Attitude Control

Proposed solar sail missions, such as the Solar Polar Orbiter [11] and the Interstellar Heliopause probe [12] have sail surface areas on the order of tens of thousands of square meters. Such large surface areas would render conventional attitude control technologies ineffective due to the large moments of inertia of these sails. Therefore, a major area of study has been focused on developing alternative means of solar sail attitude control.

To date, most solar sail missions have used conventional attitude control technologies. For example, LightSail 2 used one reaction wheel and three magnetorquers for attitude control [13]. The IKAROS spacecraft took a different approach by making use of reflectance control devices (RCD) for attitude adjustments, which controlled the voltage applied to different quadrants of its sail, demonstrating that solar radiation pressure can be used for

attitude control [5]. By adjusting the reflectivity of the sail's segments, the sail's center of pressure could be offset from the center of mass, resulting in a control torque. An active mass translation device, another technique for creating a $cm_t - cp$ offset for attitude control, was included in the NEA Scout spacecraft [14]. Should the spacecraft be recovered, the device will allow one half of the spacecraft to translate along two axes relative to the other half [14].

Aside from the successful practical demonstration of RCDs, the majority of solar sail attitude control design that incorporates the $cp - cm_t$ offset method remains largely theoretical. A variety of methods have been proposed, such as using reflective panels, known as tip vanes, attached to the sail boom tips, or a control mass attached to a two-axis gimbal mechanism [15]. If only two-axis control is desired, the spacecraft payload could be used as a gimballed control mass. Tip vane control could be added to the system if three-axis control is desired. This thesis will investigate the effectiveness of a quaternion-based PD control law for three-axis solar sail attitude control using a gimballed mass and tip vanes as actuators.

2 Background

In this section, the fundamentals of solar sailing are discussed, including the SRP force model used in this thesis as well as different solar sail configurations.

2.1 Solar Radiation Pressure Force

In interplanetary space, there are a variety of environmental forces that act on spacecraft, the largest of which is due to momentum transfer from photons, otherwise known as solar radiation pressure (SRP) [15]. The SRP, P, acting on a surface can be calculated using the following equation [15]:

$$P = \frac{W}{c} \tag{2.1}$$

where W is the radiative flux from the Sun and c is the speed of light.

The radiative flux at any distance r from the Sun is given by:

$$W = \frac{L_\odot}{4\pi r^2} \tag{2.2}$$

where $L_\odot$ is the solar luminosity and is equal to 3.84×10^{26} W [15]. It is clear from Equation (2.2) that as a solar sail moves further from the Sun, the magnitude of SRP available for sail propulsion decreases according to the inverse square law. The maximum SRP available to a solar sail at various points in the solar system is given in Figure 2.1. From this figure, it is evident that the available pressures for solar sails are extremely low. Therefore, large sail membrane surface areas are required to produce appreciable thrust forces.

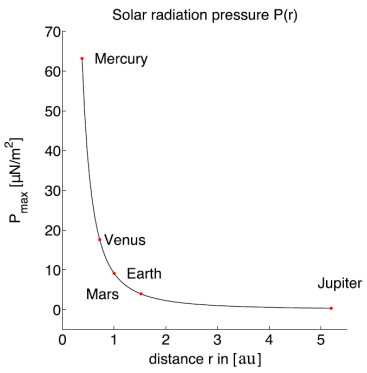

Figure 2.1: Maximum SRP for Various Locations in the Solar System [15]

When photons from the Sun encounter the sail membrane, they can be absorbed, reflected, or transmitted. Only photons that are absorbed or reflected can generate thrust. There are generally two types of SRP force models found in the literature: a realistic one that considers photon absorption and the optical properties of the sail membrane, and an ideal one that assumes all of the incident solar radiation is specularly reflected [15]. The ideal model will be employed for this thesis.

The photon-sail interaction for the ideal SRP force model is shown in Figure 2.2. Photons intercept the sail at angle α relative to the sail normal and are reflected away at the same angle. It is assumed that the sail is sufficiently far enough from the Sun such that the incident rays can be approximated as parallel rays.

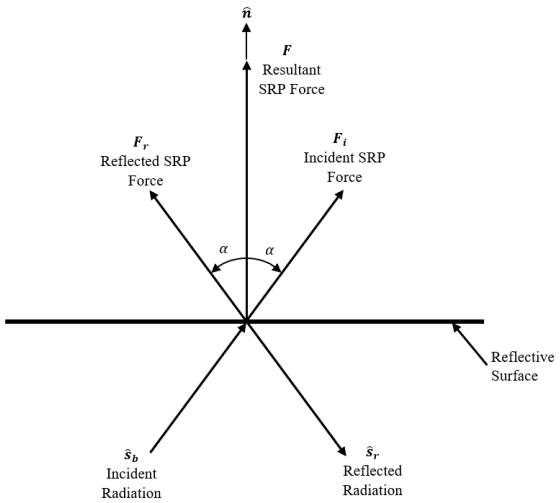

Figure 2.2: Ideal SRP Force Model

McInnes provides a derivation of the simple SRP force model in his book [16]. A similar derivation will be discussed next.

The force produced by the incident photons, $\boldsymbol{F}_i$, is given by the following equation:

$$\boldsymbol{F}_i = PA\left(\hat{\boldsymbol{s}}_b \cdot \hat{\boldsymbol{n}}\right)\hat{\boldsymbol{s}}_b \tag{2.3}$$

where A is the area of the reflective surface, $\hat{\boldsymbol{s}}_b$ is the unit Sun vector expressed in the solar sail's body frame, and $\hat{\boldsymbol{n}}$ is the anti-Sunward surface unit normal vector in the body frame. $\hat{\boldsymbol{n}}$ is always expressed as $\hat{\boldsymbol{n}} = [1, 0, 0]^T$, whereas $\hat{\boldsymbol{s}}_b$ varies over time depending on the orientation of the reflective surface. The dot product, $\hat{\boldsymbol{s}}_b \cdot \hat{\boldsymbol{n}}$ represents the reduction in sail area available to intercept photons.

The reaction force produced by the reflected photons, F_r, is equal to F_i in magnitude and is given by the following equation:

$$\boldsymbol{F}_r = -PA\left(\hat{\boldsymbol{s}}_b \cdot \hat{\boldsymbol{n}}\right)\hat{\boldsymbol{s}}_r \tag{2.4}$$

where $\hat{\boldsymbol{s}}_r$ is the unit vector in the direction of the reflected radiation.

$\boldsymbol{F}_i$ and $\boldsymbol{F}_r$ can be summed by adding their normal and tangential components. The tangential components of $\boldsymbol{F}_i$ and $\boldsymbol{F}_r$ are equal in magnitude and opposite in direction, so they cancel out. Adding the normal components together, and noting that $\cos(\alpha) = \hat{\boldsymbol{s}}_b \cdot \hat{\boldsymbol{n}}$ results in the following equation:

$$\begin{aligned}
\boldsymbol{F} &= F_{i,n} + F_{r,n} \\
&= PA\left(\hat{\boldsymbol{s}}_b \cdot \hat{\boldsymbol{n}}\right)\cos(\alpha)\hat{\boldsymbol{n}} + PA_s\left(\hat{\boldsymbol{s}}_b \cdot \hat{\boldsymbol{n}}\right)\cos(\alpha)\hat{\boldsymbol{n}} \\
&= 2PA\left(\hat{\boldsymbol{s}}_b \cdot \hat{\boldsymbol{n}}\right)^2 \hat{\boldsymbol{n}}
\end{aligned} \tag{2.5}$$

Equation (2.5) is the theoretical maximum SRP force that could be produced. There are some non-idealities related to the structure of the reflective surface that could cause

the magnitude of this force to decrease, such as membrane wrinkling and billowing. These factors are accounted for through the sail thrust coefficient, γ, which has an ideal maximum value of 2 [17]. Replacing 2 with γ in Equation (2.5) results in the following equation:

$$\boldsymbol{F} = \gamma P A \left(\hat{\boldsymbol{s}}_b \cdot \hat{\boldsymbol{n}}\right)^2 \hat{\boldsymbol{n}} \tag{2.6}$$

To express the Sun vector in the body frame, the Sun vector expressed in the orbital frame, $\hat{\boldsymbol{s}}_o$, must be multiplied by the rotation matrix, $\boldsymbol{C}_{bo}$, as follows:

$$\hat{\boldsymbol{s}}_b = \begin{bmatrix} s_{b_1} & s_{b_2} & s_{b_3} \end{bmatrix}^T = \boldsymbol{C}_{bo} \hat{\boldsymbol{s}}_o \tag{2.7}$$

In the orbital frame, $\hat{\boldsymbol{s}}_o$ is taken to be in the anti-Sunward direction and is expressed as $\hat{\boldsymbol{s}}_o = [1, 0, 0]^T$.

To avoid potential singularities introduced by using Euler angles for attitude parameterization, the solar sail's attitude will be represented using quaternions. Quaternion representation also allows computations involving the rotation matrix and kinematic equations to be carried out more efficiently than Euler angle representation due to the absence of trigonometric functions. The vector, $\boldsymbol{\epsilon}$, and scalar, η, parts of the quaternion are defined as follows:

$$\boldsymbol{\epsilon} = \boldsymbol{a} \sin\left(\frac{\phi}{2}\right) \tag{2.8}$$

$$\eta = \cos\left(\frac{\phi}{2}\right) \tag{2.9}$$

where ϕ is the principal angle of rotation of a rigid body about a principal axis $\boldsymbol{a}$. Since the attitude will use a quaternion representation, the control system will use a quaternion-based control law. Using the definitions in Equation (2.8) and Equation (2.9), the rotation matrix from the orbital frame to the spacercaft body frame can be expressed as follows:

$$\boldsymbol{C}_{bo} = \left(1 - 2\boldsymbol{\epsilon}^T \boldsymbol{\epsilon}\right) \mathbf{1} + 2\boldsymbol{\epsilon}\boldsymbol{\epsilon}^T - 2\eta\boldsymbol{\epsilon}^{\times} \tag{2.10}$$

2.2 Solar Sail Configurations

Broadly speaking, solar sails can be classified as either rigid or non-rigid sails. Rigid sails consist of a thin membrane tensioned by structural support booms that are connected to a central hub. Non-rigid sails utilize spin-induced tension to keep the membrane deployed instead of structural booms.

2.2.1 Rigid Solar Sails

Some examples of rigid solar sails include the clipper, quad sailer, and butterfly configurations. These sails are deployed from a central hub using varying numbers of structural support booms. The clipper configuration features four quadrants, each of which contains a membrane segment and two support spars [15]. The quad sailer configuration features two spars per quadrant, which could allow for individual adjustability of each membrane segment for attitude control purposes [15]. The butterfly configuration only uses two spars, resulting in a lower structural mass than the other two variants, however it generally has a smaller surface area than other rigid sail designs [15]. These designs are shown in Figure 2.3.

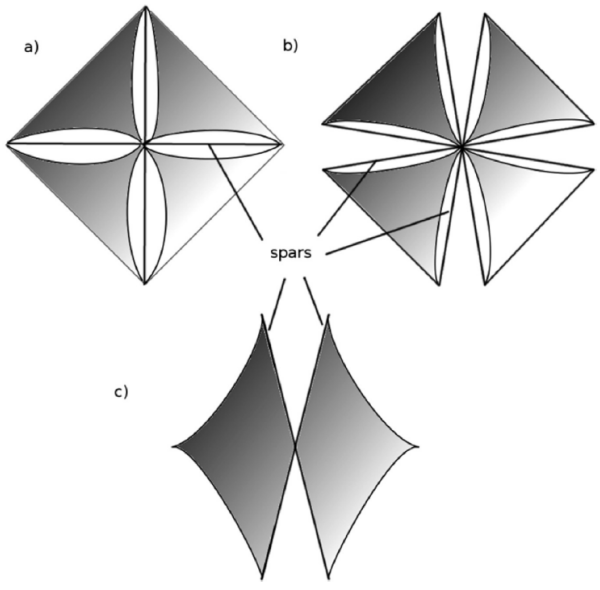

Figure 2.3: Rigid Solar Sail Designs (a: clipper, b: quad sailer, c: butterfly) [18]

2.2.2 Non-Rigid Solar Sails

The two primary non-rigid solar sail designs include the disk-type sail and the heliogyro. The disk-type sail deploys and remains taut by spinning about the sail's roll axis and was successfully demonstrated in the IKAROS mission discussed in Section 1 [5]. The heliogyro concept was first proposed in 1969 and utilizes long reflective blades that also deploy by spinning the sail [19]. Each blade can be rotated about its lengthwise axis to control the magnitude and direction of the SRP forces acting on them [19]. These designs offer the advantage of having lower masses than the rigid sails since they do not require any structural booms. These designs are shown in Figures 2.4(a) and 2.4(b), respectively.

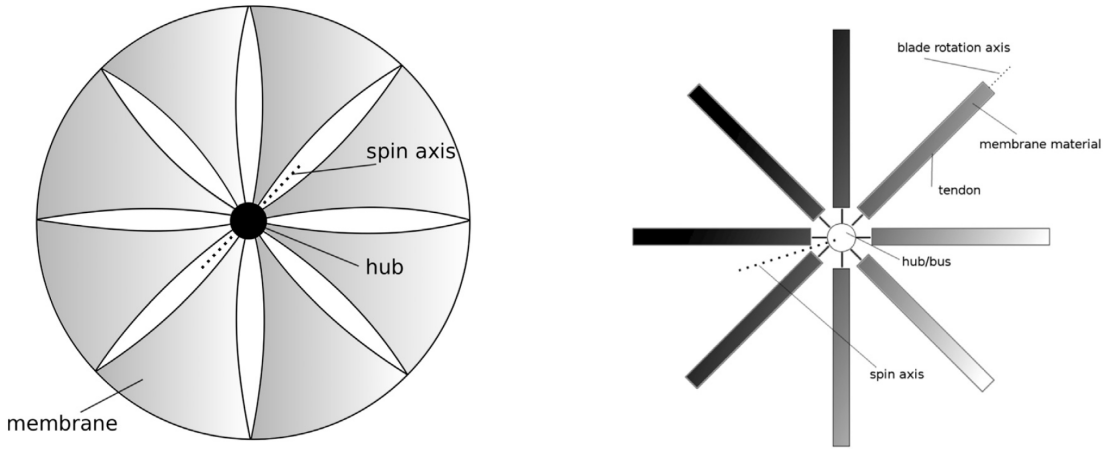

(a) Disk Sail Design [15] (b) Heliogyro Sail Design [18]

Figure 2.4: Non-Rigid Solar Sail Designs

3 Attitude Control Techniques

This section begins by discussing the challenges associated with using conventional techniques for solar sail attitude control and the motivation for researching alternative methods. It then details current research into rigid solar sail attitude control techniques, including the advantages and disadvantages associated with each technique.

3.1 Challenges with Conventional Techniques

Conventional spacecraft attitude control strategies are largely ineffective for solar sails. Sail membrane surface areas can be quite large, and as a result, SRP disturbance torques acting on solar sails are significantly greater than those acting on typical Earth-orbiting satellites. For example, a 40 $\times$ 40 m, 160 kg sail with a $cm_t - cp$ offset of $\pm$ 0.1 m experiencing an SRP force of 0.01 N has an SRP disturbance torque of $\pm$ 0.001 Nm, which is about 100 times larger than those acting on typical geosynchronous Earth-orbiting satellites [17]. This issue is compounded by the fact that a solar sail's mass is spread out over a large area, resulting in high moments of inertia. The necessary control torques would require large conventional actuators, such as reaction wheels, which is impractical for a solar sail. In addition, controlling solar sail attitude using onboard propellant would also prove ineffective since, unlike SRP, propellant is an expendable resource and would not be ideally suited for the long duration missions proposed for solar sails [15]. Therefore, it is desirable to find alternative techniques for solar sail attitude control that can overcome these challenges.

3.2 Approaches to Solar Sail Attitude Control

A major area of solar sail research is the design of control systems that utilize SRP to regulate the orientation and angular velocities of solar sails. The idea of using SRP for spacecraft attitude control was first proposed by Sohn in 1959, and since then, various techniques have been studied for both rigid and non-rigid solar sails [20]. Most of the proposed approaches

for rigid solar sail attitude control generally involve creating an offset between the solar sail's center of mass and center of pressure to generate control torques about the sail's center of mass. Approaches for non-rigid solar sail attitude control focus on shifting the sail's center of pressure [15]. The remainder of this section will focus on attitude control techniques for rigid solar sails.

3.2.1 Gimballed Mass Method

First proposed by Angrilli and Bortolami, the gimballed mass method uses a control mass attached to the end of a rod, which is articulated using a gimbal mechanism attached to the sail's central hub as shown in Figure 3.1 [21]. This figure shows the system's center of mass lying in the sail plane. Depending on the mass attached to the end of the rod, this may not be a reasonable assumption and the center of mass could lie out-of-plane. The rod possesses two degrees of freedom and can be commanded to different locations described by the gimbal clock, ϕ_g, and cone, θ_g, angles.

Initially, when the rod is perpendicular to the sail plane, the system's cm_t and cp coincide with each other, but as the rod is commanded to different locations, the cm_t is offset from the cp, and a control torque about the cm_t is generated. As a result, the sail membrane functions as a type of gimballed engine for the spacecraft. Since the motion of the gimballed mass is constrained to two degrees of freedom, this approach is unable to generate control torques about the sail's roll axis without performing a sequence of rotations about the solar sail's principal axes [22].

Current research into control system design using a gimballed mass has focused on using a linear-quadratic regulator (LQR) for attitude control [23] [24] [25]. While this is acceptable for small angles and rates, it would be ineffective for larger ones since the LQR approach uses linearized equations of motion. Therefore, it is of interest to design a gimballed mass control system that uses nonlinear equations of motion. Sperber et al. developed a control scheme that uses nonlinear equations of motion and a 1-2-1 Euler sequence to provide three-axis

control [22].

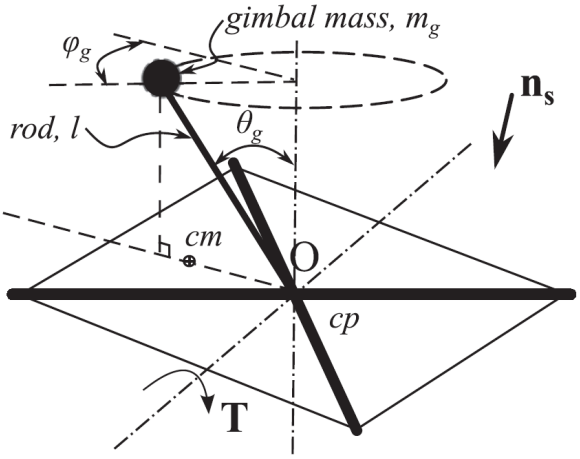

Figure 3.1: Solar Sail with a Gimballed Mass [15]

3.2.2 Sliding Masses Method

This method uses two sliding masses, labelled as m_{s_1} and m_{s_2} in Figure 3.2, that translate along the sail booms. When both masses move away from the center of the sail, the system's cm_t is offset from the cp, which exerts a control torque on the spacecraft. Like the gimballed mass method, this approach can only produce torques about the sail's pitch and yaw axes. Wie and Murphy developed an attitude control system using this method in conjunction with tilted sail segments for roll axis control [26]. They validated the effectiveness of this control system by simulating a 35-degree yaw maneuver and showing that the roll and pitch attitude errors remained small, and the control actuators remained within their saturation limits [26]. Adeli et al. designed a system that employed this method with reflective panels for roll axis control and showed that the design could be scaled for a variety of missions, such as the interstellar heliopause probe [27].

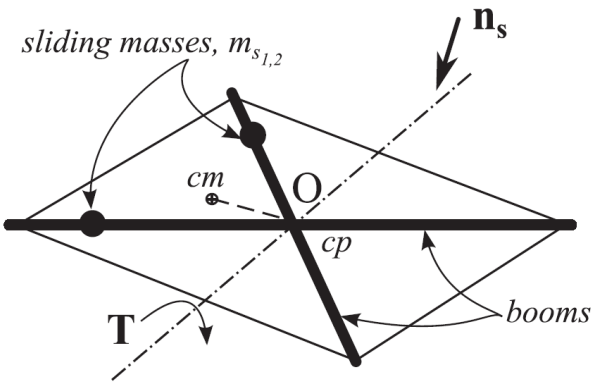

Figure 3.2: Solar Sail with Sliding Masses [15]

3.2.3 Tip Vane Method

The tip vane method typically utilizes four additional membrane segments that are connected to the tips of each boom as shown in Figure 3.3. These vanes are made of the same material as the sail and are generally triangular. Each vane possesses up to two degrees of freedom, so only two vanes located on opposite sides of the sail are necessary to achieve three-axis control, although the two additional vanes add redundancy to the system.

The tip vane method has been studied extensively in the literature. Wie studied this method and derived the equations of motion for four single-degree-of-freedom tip vanes [23]. A solar sail equipped with four two degree-of-freedom tip vanes would have eight control inputs. Since only three control torques need to be determined for three-axis control, this results in an under-constrained control allocation problem. To address this problem, Choi and Damaren developed a method that determines a set of vane angles based on the desired torque and current Sun angles [28]. Tip vanes could be used to supplement other two degree-of-freedom control approaches, such as the gimballed mass method. Bladt and Lawrence simulated a control system that used a gimballed mass combined with two opposing tip vanes to generate a "windmill" torque about the sail's roll axis [29]. Using this approach, they found that vane angles of less than one degree were required to achieve the desired roll torques.

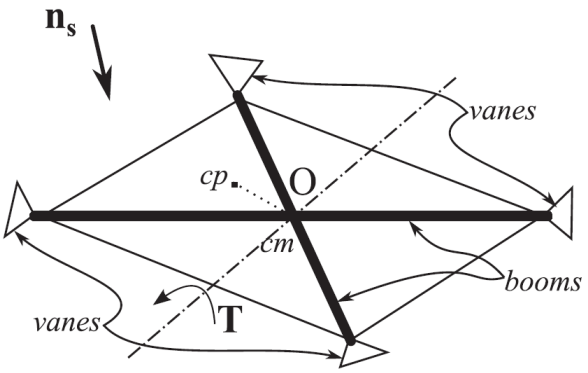

Figure 3.3: Solar Sail with Four Control Vanes [15]

3.2.4 Tilted Wings Method

The tilted wings method involves attaching adjacent sail membranes to tip bars on the ends of each boom. These rods can be rotated about the boom axes to shift the sail membranes out of the sail plane as shown in Figure 3.4. This approach is only able to generate control torques about a sail's roll axis, so to achieve three-axis control, it must be combined with another approach, such as the shifted wings method, which involves retracting and extending sail membrane segments towards and from the sail's central hub. Wie developed a PID control system using a combination of the tilted and shifted wing methods [23].

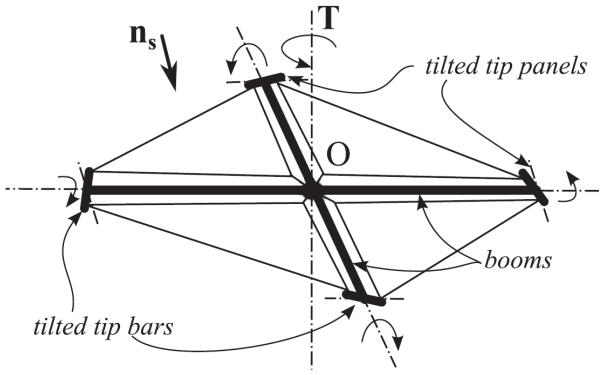

Figure 3.4: Solar Sail with Tilted Wings [15]

4 Objectives

From the preceding sections, it has become apparent that large solar sails require a more unconventional means of attitude control than traditional spacecraft for long duration missions due to their large moments of inertia. Therefore, the overarching objective of this thesis is to evaluate the effectiveness of a quaternion-based PD law for three-axis attitude control of a solar sail that utilizes a gimballed mass and control vanes as actuators. This will be accomplished by simulating the system in MATLAB under a variety of initial conditions. The simulations performed for this investigation will incorporate the effects of second-order actuator dynamics to understand their impact on the control system's performance. The main thesis objective will be achieved by carrying out the research in three phases:

1. Phase 1 will involve developing a simulator that models two-axis control of a solar sail using only a gimballed mass actuator.

2. Phase 2 will involve developing a simulator that models three-axis control of a solar sail by integrating tip vanes into the spacecraft's control system.

3. Phase 3 will involve performing parametric studies to determine the effects of varying some of the input parameters, such as gimballed payload mass or tip vane surface area, on the control system performance.

5 Solar Sail Control Model

In this section, the equations governing the solar sail's dynamics are presented along with the control law for the system. The procedure used for simulating the sail's dynamics is also discussed.

5.1 Assumptions

To simplify the analyses, the following assumptions were made:

1. The simulation durations are short enough such that degradation of sail membrane optical properties is considered negligible.

2. The simulation durations are short enough such that the Sun vector remains constant in the orbital reference frame.

3. The gimballed payload can be approximated as a point mass.

4. The gimballed rod's radius is much smaller than its length and can be approximated as a long slender rod for moment of inertia calculations.

5. The solar sail film, central hub, gimbal mechanism, and booms can be approximated as a thin rigid plate.

6. Other environmental disturbance forces acting on the sail, such as those due to solar wind, are considered negligible compared to the SRP force.

7. The effect of any shadowing of the sail membrane on the SRP forces generated is considered negligible.

8. The solar sail is orbiting the Sun at 1 AU, which is sufficiently far enough from the Sun such that incident solar radiation can be approximated as parallel rays.

9. All of the solar radiation incident on the sail's reflective face is specularly reflected.

10. None of the solar radiation incident on the sail's emissive face is reflected. Any forces produced due to absorption or emission of solar radiation on this face are considered negligible.

11. The solar sail uses the clipper design discussed in Section 2.2.1.

5.2 Solar Sail Dynamic Model

As shown in Figure 5.1 and Figure 5.2, the system consists of a square sail membrane tensioned by four structural support booms that deploy from a central hub. An altitude-azimuth style gimbal mechanism driven by two DC motors is mounted to the central hub and controls the position of a rod with a tip-mounted payload. Two SDOF tip vanes also driven by DC motors are mounted to opposite ends of one of the sail's support booms and are made of the same material as the main sail. The gimballed rod and payload are located on the anti-Sunward face of the sail to reduce the effect of shadowing on the amount of thrust generated by the sail. The anti-Sunward face of the sail membrane acts as a radiator for temperature regulation and is covered in a black emissive coating. One side of each of the tip vanes is also covered in the same coating. Since the primary function of a spacecraft radiator is to reject heat into space, it is desired that the black emissive side never faces the Sun. If this were to happen, it would be considered a failure of the control system.

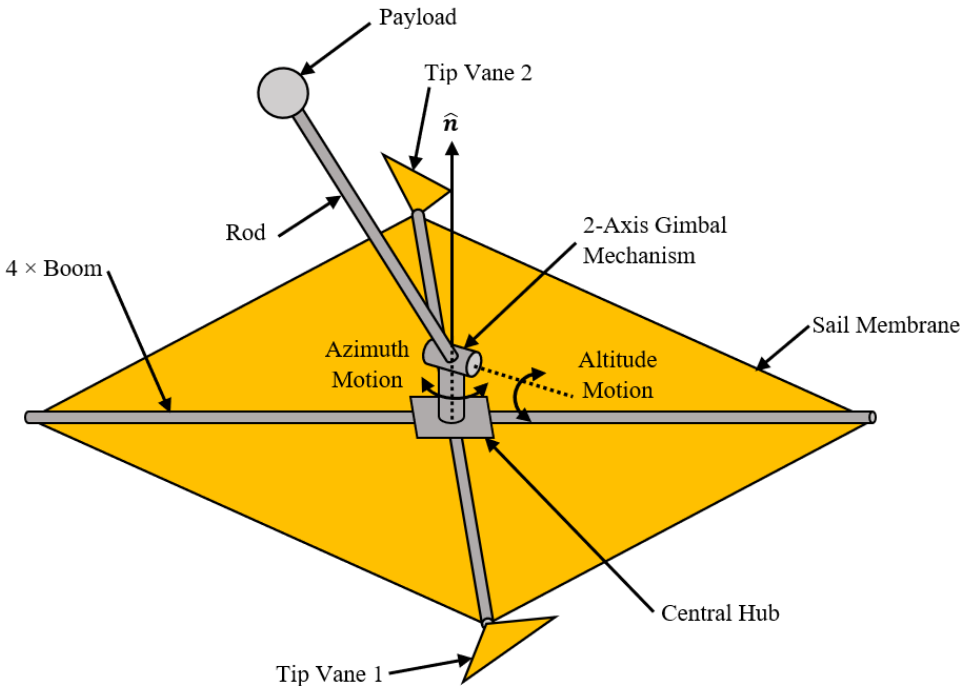

Figure 5.1: Solar Sail System Model

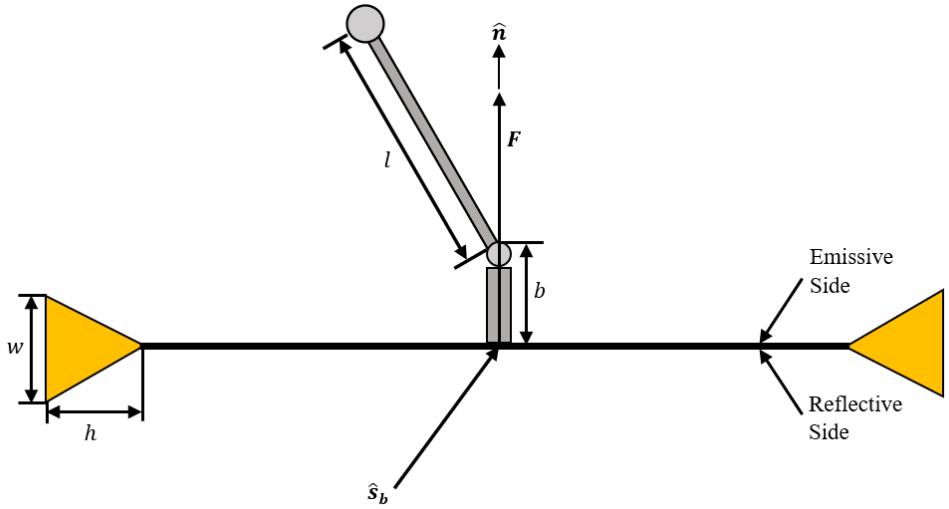

Figure 5.2: Solar Sail Side View

The ST7 solar sail parameters used by Wie were also used for this thesis [23]. This gimballed rod mass used in the ODISSEE solar sail concept was also used [30]. These parameters are shown in Table 5.1. The tip vane dimensions were chosen as baseline values for the simulations performed in Phases 1 and 2.

Table 5.1: Solar Sail Parameters

Parameter	**Value**
Sail Side Length (a)	40 m
Gimballed Rod Length (l)	2 m
Individual Tip Vane Area (A_{tv})	20 m^2
Tip Vane Width (w)	5 m
Tip Vane Height (h)	8 m
Sail Area (A_s)	1400 m^2
Thrust Coefficient (γ)	1.816
Gimbal Mechanism Height (b)	0.5 m
Sail Film Mass (m_f)	6.1 kg
Individual Boom Mass (m_b)	3.575 kg
Central Hub Mass (m_h)	19.6 kg
Sail Subsystem Mass (m_s)	$m_f + 4m_b + m_h = 40$ kg
Payload Mass (m_p)	116 kg
Gimballed Rod Mass (m_r)	4 kg
Individual Tip Vane Mass (m_{tv})	$(m_f/A_s)\, A_{tv} \approx 0.09$ kg
Total Mass (m_t)	$m_s + m_p + m_r + 2m_{tv} \approx 160.17$ kg

The solar sail's angular velocity dynamics can be described by Euler's equation for rotational motion as follows:

$$\boldsymbol{I}\dot{\boldsymbol{\omega}} + \boldsymbol{\omega}^{\times}\boldsymbol{I}\boldsymbol{\omega} = \boldsymbol{T}_c \tag{5.1}$$

where $\boldsymbol{I}$ is the sail's time-varying moment of inertia matrix, $\boldsymbol{\omega} = [\omega_1, \omega_2, \omega_3]^T$ is the column vector containing the sail's angular velocity vector components expressed in the body frame, and $\boldsymbol{T}_c = [T_{b_1}, T_{b_2}, T_{b_3}]^T$ is the column vector containing the control torques acting about each of the sail's body axes. Equation (5.1) uses the spacecraft's composite center of mass, cm_t, as a reference point. Wie took a different approach and instead used the sail subsystem's center of mass as the reference point for the dynamical equations of motion [23].

5.3 Quaternion PD Control

For this thesis, a quaternion PD control law will be implemented for the reasons outlined in Section 2.1. Since the desired angular velocity components of the solar sail are all zero, the

desired control torques are given by

$$\boldsymbol{T}_{c,d} = -K_p \boldsymbol{\epsilon}_e - K_d \boldsymbol{\omega} \tag{5.2}$$

where K_p and K_d are the proportional and derivative control gains, respectively, and $\boldsymbol{\epsilon}_e$ is the vector part of the error quaternion. The vector part of the error quaternion is given by

$$\boldsymbol{\epsilon}_e = \left(\eta_d \mathbf{1} - \boldsymbol{\epsilon}_d^{\times}\right) \boldsymbol{\epsilon} - \boldsymbol{\epsilon}_d \eta \tag{5.3}$$

where $\boldsymbol{\epsilon}$ is the vector part of the current quaternion, η_d is the scalar component of the desired quaternion, and $\boldsymbol{\eta}_d$ is the vector part of the desired quaternion.

The current angular velocities are calculated by substituting Equation (5.2) into Equation (5.1) for $\boldsymbol{T}_{c,d}$ and numerically integrating the following result:

$$\dot{\boldsymbol{\omega}} = \boldsymbol{I}^{-1} \left(-\boldsymbol{\omega}^{\times} \boldsymbol{I} \boldsymbol{\omega} - K_p \boldsymbol{\epsilon}_e - K_d \boldsymbol{\omega}\right) \tag{5.4}$$

The current values of the scalar and vector components of the quaternion are calculated by numerically integrating the following kinematic relationship:

$$\dot{\boldsymbol{q}} = \begin{bmatrix} \dot{\boldsymbol{\epsilon}} \\ \dot{\eta} \end{bmatrix} = \frac{1}{2} \begin{bmatrix} \eta \mathbf{1} + \boldsymbol{\epsilon}^{\times} \\ -\boldsymbol{\epsilon}^T \end{bmatrix} \boldsymbol{\omega} \tag{5.5}$$

where η is the current scalar component of the quaternion.

The controller gains, K_p and K_d, were determined to be 9.9×10^{-3} Nm and 2.2 Nm/rad/s, respectively. These gains were selected using trial and error to minimize overshoot and settling time.

5.4 Gimbal Angle Calculation

Once the necessary gimbal control torques have been calculated using Equation (5.2), the gimbal clock and cone angles, ϕ_g and θ_g, can be calculated using the s_{b1} component of the sun vector and the $cm_t - cp$ offset distance. The orthogonal distances from $\boldsymbol{F}$ to the b_2 and b_3 axes can be calculated by determining the cm_t location using the geometry shown in Figure 5.3. Note that the frame located at cm_s is used for calculating the center of mass location, while the frame located at cm_t is used for calculating the moment of inertia matrix.

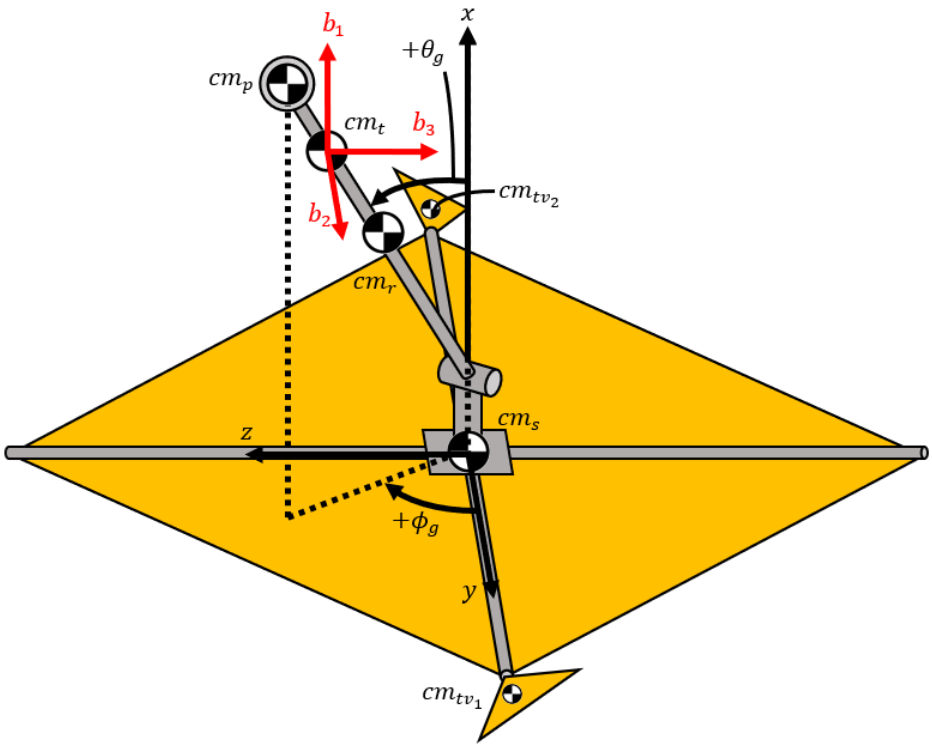

Figure 5.3: Locations of System Mass Centers

The cm_t location can be calculated using the definition of the center of mass as follows:

$$cm_t = (x_{cm_t}, y_{cm_t}, z_{cm_t}) = \left(\frac{\sum_{i=1}^{n} x_i m_i}{m_t}, \frac{\sum_{i=1}^{n} y_i m_i}{m_t}, \frac{\sum_{i=1}^{n} z_i m_i}{m_t} \right) \tag{5.6}$$

where x_{cm_t}, y_{cm_t}, and z_{cm_t} are the x, y, and z coordinates of the system center of mass; n is the number of mass centers that the system is divided into, which in this case is 3; x_i, y_i,

and z_i are the x, y, and z distances from the each mass center to the origin, which in this case is chosen to be the sail subsystem mass center, cm_s; m_i are the component masses of the system; and m_t is the total system mass.

Combining the geometry from Figure 5.3 with the definition of cm_t in Equation (5.6) yields the following results:

$$x_{cm_t} = \left(\frac{b + l\cos(\theta_g)}{m_t}\right)\left(m_p + \frac{m_r}{2}\right) \tag{5.7}$$

$$y_{cm_t} = \left(\frac{l\sin(\theta_g)\cos(\phi_g)}{m_t}\right)\left(m_p + \frac{m_r}{2}\right) \tag{5.8}$$

$$z_{cm_t} = \left(\frac{l\sin(\theta_g)\sin(\phi_g)}{m_t}\right)\left(m_p + \frac{m_r}{2}\right) \tag{5.9}$$

Since cm_t is located at the origin, the only contribution of m_s to the composite center of mass location is through m_t. Since the tip vanes are located on opposite sides of the sail, their only contribution to the composite center of mass is also through m_t.

Once the center of mass location is determined, the control torques about the b_2 and b_3 axes can also be calculated using the following equations:

$$T_{g,b_2} = \|\boldsymbol{F}\| z_{cm_t} = \gamma P A_s s_{b_1}^2 z_{cm_t} \tag{5.10}$$

$$T_{g,b_3} = \|\boldsymbol{F}\| y_{cm_t} = \gamma P A_s s_{b_1}^2 y_{cm_t} \tag{5.11}$$

Substituting Equation (5.9) into Equation (5.10) for z_{cm_t} and substituting Equation (5.8) into Equation (5.11) for y_{cm_t} then solving the resulting system of equations for ϕ_g and θ_g yields the following results:

$$\phi_g = \arctan\left(\frac{T_{b_2}}{T_{b_3}}\right) \tag{5.12}$$

$$\theta_g = \arcsin\left(\frac{T_{b_3} m_t}{\gamma P A_s s_{b_1}^2 l\cos(\phi_g)\left(m_p + \frac{m_r}{2}\right)}\right) \tag{5.13}$$

As a result of the inverse trigonometric functions in these equations, the ranges of ϕ_g and

θ_g are [-90°,+90°]. Another result of the inverse sine in Equation (5.13) is a restriction on its argument. Since the domain of the inverse sine function is [-1,1], the absolute value of the numerator must be less than or equal to the absolute value of the denominator. This places a potential limitation on the system. If the desired control torque about the b_3 axis is too large, it may result in the argument of Equation (5.13) falling outside of the [-1,1] domain. In this case, no set of ϕ_g and θ_g angles would be capable of generating the desired torques. Equation (5.2) shows a dependence of the control torques on the angular velocities. Therefore, it is possible for large angular velocities to result in control torques that cannot be generated.

If no set of gimbal angles capable of generating the desired torques can be determined, the control system commands the gimbal to move to a cone angle of ±90° depending on the value of the argument of Equation (5.13). If the argument is greater than 1, then the cone angle is commanded to +90°, since this would result in the largest possible torque for a given sail orientation. Similarly, if the argument is less than -1, the cone angle is commanded to -90°.

If the spacecraft's emissive side faces the Sun, the gimballed payload would be unable to generate any significant torques due to the low reflectivity of the sail's emissive side. To model this in the simulation, the gimbal torques are set to zero when the sun vector in the body frame becomes negative. The gimbal angles are also set to zero in this case since it is not necessary to have the motors continue to move when the gimballed payload cannot generate any significant torques.

5.5 Tip Vane Angle Calculation

As shown in Figure 5.1, the two SDOF tip vanes can be rotated to produce "windmill" torques about the spacecraft's b_1 axis. Since the system's composite center of mass does not remain at the center of the sail plane, these tip vane orientations will also generate torques about the b_2 and b_3 axes. The sign conventions adopted for the tip vane angles are shown

in Figure 5.4.

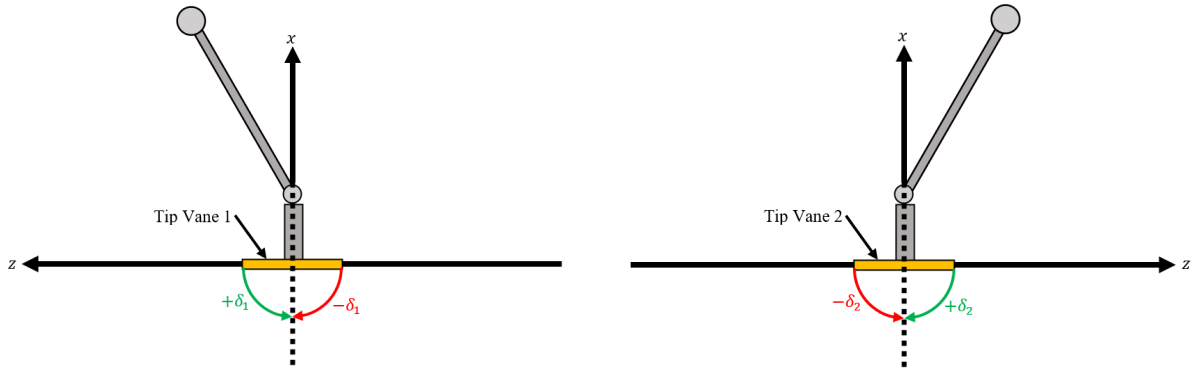

(a) Tip Vane 1 Angle (b) Tip Vane 2 Angle

Figure 5.4: Tip Vane Angle Sign Conventions

The torques generated by a single tip vane can be calculated by taking the cross product of the tip vane moment arm and the SRP force as follows:

$$\boldsymbol{T}_{tv_i} = \boldsymbol{l}_{tv_i} \times \boldsymbol{F} = \boldsymbol{l}_{tv_i}^{\times} \boldsymbol{F} \tag{5.14}$$

where $\boldsymbol{T}_{tv_i}$ is the torque produced by the ith tip vane and $\boldsymbol{l}_{tv_i}$ is the ith tip vane moment arm.

The tip vane anti-Sunward surface unit normal vectors in the body frame are expressed as follows:

$$\hat{\boldsymbol{n}}_{tv_1,b} = \begin{bmatrix} \cos(\delta_1) & 0 & \sin(\delta_1) \end{bmatrix}^T \tag{5.15}$$

$$\hat{\boldsymbol{n}}_{tv_2,b} = \begin{bmatrix} \cos(\delta_2) & 0 & \sin(\delta_2) \end{bmatrix}^T = \begin{bmatrix} \cos(-\delta_1) & 0 & \sin(-\delta_1) \end{bmatrix}^T \tag{5.16}$$

For Equation (5.16), the relation $\delta_2 = -\delta_1$ has been used. This is done to make it possible to solve for the tip vane angles using the desired b_1 axis control torque since there would otherwise be one torque equation and two unknown angles. For a given value of δ_1, tip vane 2 rotates by the same amount in the opposite direction.

The moment arms for the two tip vanes are calculated as follows:

$$\boldsymbol{l}_{tv_1} = \begin{bmatrix} l_{tv_1,x} & l_{tv_1,y} & l_{tv_1,z} \end{bmatrix}^T = \begin{bmatrix} -x_{cm_t} & \left(\frac{a\sqrt{2}}{2} + \frac{2}{3}h\right) - y_{cm_t} & z_{cm_t} \end{bmatrix}^T \tag{5.17}$$

$$\boldsymbol{l}_{tv_2} = \begin{bmatrix} l_{tv_2,x} & l_{tv_2,y} & l_{tv_2,z} \end{bmatrix}^T = \begin{bmatrix} -x_{cm_t} & -\left(\frac{a\sqrt{2}}{2} + \frac{2}{3}h\right) - y_{cm_t} & z_{cm_t} \end{bmatrix}^T \tag{5.18}$$

Using Equation (5.14) along with Equations (2.6), (5.15), (5.16), (5.17), and (5.18), we can obtain Equations (5.19) and (5.20) for the torques produced by tip vanes 1 and 2, respectively:

$$\boldsymbol{T}_{tv_1} = \gamma P A_{tv} \left[s_{b_1}\cos(\delta_1) - s_{b_3}\sin(\delta_1)\right]^2 \begin{bmatrix} -\sin(\delta_1) l_{tv_1,y} \\ \cos(\delta_1) l_{tv_1,z} + \sin(\delta_1) l_{tv_1,x} \\ -\cos(\delta_1) l_{tv_1,y} \end{bmatrix} \tag{5.19}$$

$$\boldsymbol{T}_{tv_2} = \gamma P A_{tv} \left[s_{b_1}\cos(\delta_1) + s_{b_3}\sin(\delta_1)\right]^2 \begin{bmatrix} \sin(\delta_1) l_{tv_2,y} \\ \cos(\delta_1) l_{tv_2,z} - \sin(\delta_1) l_{tv_2,x} \\ -\cos(\delta_1) l_{tv_2,y} \end{bmatrix} \tag{5.20}$$

Adding Equation (5.19) and Equation (5.20) together gives the total torque vector produced by both tip vanes:

$$\begin{aligned} \boldsymbol{T}_{tv_{total}} = \gamma P A_{tv} \Bigg(& \left[s_{b_1}\cos(\delta_1) - s_{b_3}\sin(\delta_1)\right]^2 \begin{bmatrix} -\sin(\delta_1) l_{tv_1,y} \\ \cos(\delta_1) l_{tv_1,z} + \sin(\delta_1) l_{tv_1,x} \\ -\cos(\delta_1) l_{tv_1,y} \end{bmatrix} + \\ & \left[s_{b_1}\cos(\delta_1) + s_{b_3}\sin(\delta_1)\right]^2 \begin{bmatrix} \sin(\delta_1) l_{tv_2,y} \\ \cos(\delta_1) l_{tv_2,z} - \sin(\delta_1) l_{tv_2,x} \\ -\cos(\delta_1) l_{tv_2,y} \end{bmatrix} \Bigg) \end{aligned} \tag{5.21}$$

From (5.21), the torque produced about the b_1 axis is given by:

$$\begin{aligned} T_{tv,b_1} = \gamma P A_{tv} \sin(\delta_1) \big(& l_{tv_2,y} \left[s_{b_1}\cos(\delta_1) + s_{b_3}\sin(\delta_1)\right]^2 - \\ & l_{tv_1,y} \left[s_{b_1}\cos(\delta_1) - s_{b_3}\sin(\delta_1)\right]^2 \big) \end{aligned} \tag{5.22}$$

The tip vane 1 angle, δ_1, can be calculated from (5.22) using a Weierstrass substitution, which is defined as follows:

$$t = \tan\left(\frac{\delta_1}{2}\right) \tag{5.23}$$

Using Equation (5.23), the following relationships can be obtained:

$$\sin(\delta_1) = \frac{2t}{1+t^2} \qquad\qquad \cos(\delta_1) = \frac{1-t^2}{1+t^2} \tag{5.24}$$

Substituting the relationships from (5.24) into Equation (5.22) yields the following:

$$T_{tv,b_1} = \gamma P A_{tv}\left(\frac{2t}{1+t^2}\right)\left(l_{tv_2,y}\left[s_{b_1}\left(\frac{1-t^2}{1+t^2}\right) + s_{b_3}\left(\frac{2t}{1+t^2}\right)\right]^2 - l_{tv_1,y}\left[s_{b_1}\left(\frac{1-t^2}{1+t^2}\right) - s_{b_3}\left(\frac{2t}{1+t^2}\right)\right]^2\right) \tag{5.25}$$

Simplifying Equation (5.25) yields the following:

$$0 = a_6 t^6 + a_5 t^5 a_4 t^4 + a_3 t^3 + a_2 t^2 + a_1 t + a_0 \tag{5.26}$$

where the above coefficients are equal to:

$$\begin{aligned}
a_0 &= -T_{tv,b1} \\
a_1 &= 2\gamma P A_{tv} s_{b_1}^2 \left(l_{tv_2,y} - l_{tv_1,y}\right) \\
a_2 &= 8\gamma P A_{tv} s_{b_1} s_{b_3} \left(l_{tv_1,y} + l_{tv_2,y}\right) \\
a_3 &= 2\gamma P A_{tv} \left(4s_{b_3}^2 - 2s_{b_1}^2\right)\left(l_{tv_2,y} - l_{tv_1,y}\right) \\
a_4 &= -8\gamma P A_{tv} s_{b_1} s_{b_3} \left(l_{tv_1,y} + l_{tv_2,y}\right) - 3T_{tv,b_1} \\
a_5 &= 2\gamma P A_{tv} s_{b_1}^2 \left(l_{tv_2,y} - l_{tv_1,y}\right) \\
a_6 &= -T_{tv,b_1}
\end{aligned}$$

The roots function in MATLAB was used to solve Equation (5.26) for the roots of the sixth-order polynomial. To extract a viable tip vane angle from these roots, a three-step filtering process was employed.

The first step involves checking whether the roots of the polynomial are real or complex. Any complex roots are filtered out and the real roots are converted into tip vane angles using the definition of the Weierstrass substitution:

$$t = \tan\left(\frac{\delta_1}{2}\right) \Rightarrow \delta_1 = 2\arctan(t) \tag{5.27}$$

The second step involves checking if the tip vane angle candidates that were calculated using Equation (5.27) lie within the range [-90°,90°] and if the dot product of the tip vane normal vector in the body frame and the Sun vector in the body frame is greater than or equal to zero, i.e., $\hat{\boldsymbol{s}}_b \cdot \hat{\boldsymbol{n}}_{tv_1,b} \geq 0$. This second condition is necessary to ensure the emissive sides of the tip vanes do not face the Sun.

If the number of real roots is equal to the number of angles filtered out in the second step, or if all the roots are complex, then there exists no valid tip vane angle that can generate the desired control torques and δ_1 is set to zero. If there are some angles that are not filtered out in the second step, then a third step in the filtering process is executed where the absolute value of the difference between each angle candidate and the previous tip vane angle is calculated. Whichever tip vane angle candidate produces the smallest difference will become the next tip vane angle.

5.6 Moment of Inertia Matrix Calculation

Since $\boldsymbol{I}$ in Equation (5.1) is calculated with respect to the spacecraft's center of mass, as the spacecraft's center of mass changes due to the gimballed rod's motion, $\boldsymbol{I}$ also changes and needs to be recalculated at each time step of the simulation. When calculating the moment of inertia matrix, the sail membrane is assumed to be a flat plate, the gimballed

rod is assumed to be a long slender rod, i.e., the rod's radius is assumed to be much smaller than its length, the gimballed payload is assumed to be a point mass, and the tip vanes are assumed to be flat triangular plates.

To calculate the overall moment of inertia matrix, it is necessary to first calculate the moment of inertia matrices of each component in the system separately in each of their respective frames.

The moment of inertia matrix for the sail subsystem in the sail frame, which includes mass contributions from the central hub and support booms, is calculated as follows:

$$\boldsymbol{I}_s = \frac{m_s}{12}\begin{bmatrix} 2a^2 & 0 & 0 \\ 0 & a^2 & 0 \\ 0 & 0 & a^2 \end{bmatrix} \tag{5.28}$$

The moment of inertia matrix for the gimballed rod in the gimbal frame is calculated as follows:

$$\boldsymbol{I}_r = \frac{m_r l^2}{12}\begin{bmatrix} 0 & 0 & 0 \\ 0 & 1 & 0 \\ 0 & 0 & 1 \end{bmatrix} \tag{5.29}$$

The moment of inertia matrix for each tip vane in the tip vane frame is calculated as follows:

$$\boldsymbol{I}_{tv} = \frac{m_{tv}}{36}\begin{bmatrix} 2\left(h^2 + 0.75w^2\right) & 0 & 0 \\ 0 & 1.5w^2 & 0 \\ 0 & 0 & 2h^2 \end{bmatrix} \tag{5.30}$$

Once the component moment of inertia matrices are calculated in their respective frames, the rotational transformation theorem for inertia matrices is used to express these matrices in the spacecraft body frame as follows:

$$\boldsymbol{I}_b = \boldsymbol{C}_{bc}\boldsymbol{I}_c\boldsymbol{C}_{bc}^T \tag{5.31}$$

where $\boldsymbol{I}_b$ is the moment of inertia matrix of the component with respect to the spacecraft body frame, $\boldsymbol{C}_{bc}$ is the rotation matrix from the component frame to the spacecraft body

frame, and $\boldsymbol{I}_c$ is the moment of inertia matrix of the component with respect to the the component frame.

The rotation matrix from the sail frame to the spacecraft body frame, $\boldsymbol{C}_{bs}$, describes a rotation of 45°about the b_1 axis and is given by:

$$\boldsymbol{C}_{bs} = \begin{bmatrix} 1 & 0 & 0 \\ 0 & \cos(45) & -\sin(45) \\ 0 & \sin(45) & \cos(45) \end{bmatrix} = \begin{bmatrix} 1 & 0 & 0 \\ 0 & \frac{\sqrt{2}}{2} & -\frac{\sqrt{2}}{2} \\ 0 & \frac{\sqrt{2}}{2} & \frac{\sqrt{2}}{2} \end{bmatrix} \tag{5.32}$$

The rotation matrix from the gimbal frame to the spacecraft body frame, $\boldsymbol{C}_{bg}(-\theta_g, \phi_g)$, describes a sequence of two rotations: first, a rotation of -θ_g degrees about the gimbal's b_3 axis, then a subsequent rotation of ϕ_g degrees about the intermediate b_1 axis. This matrix is expressed as follows:

$$\begin{aligned} \boldsymbol{C}_{bg}(-\theta_g, \phi_g) &= \boldsymbol{C}_{b_1}(\phi_g)\,\boldsymbol{C}_{b_3}(-\theta_g) \\ &= \begin{bmatrix} 1 & 0 & 0 \\ 0 & \cos(\phi_g) & -\sin(\phi_g) \\ 0 & \sin(\phi_g) & \cos(\phi_g) \end{bmatrix} \begin{bmatrix} \cos(-\theta_g) & -\sin(-\theta_g) & 0 \\ \sin(-\theta_g) & \cos(-\theta_g) & 0 \\ 0 & 0 & 1 \end{bmatrix} \\ &= \begin{bmatrix} \cos(-\theta_g) & -\sin(-\theta_g) & 0 \\ \sin(-\theta_g)\cos(\phi_g) & \cos(-\theta_g)\cos(\phi_g) & -\sin(\phi_g) \\ \sin(-\theta_g)\sin(\phi_g) & \cos(-\theta_g)\sin(\phi_g) & \cos(\phi_g) \end{bmatrix} \end{aligned} \tag{5.33}$$

The rotation matrix from the tip vane 1 frame to the spacecraft body frame, $\boldsymbol{C}_{bv_1}(-\delta_1)$, describes a rotation of -δ_1 degrees about the b_2 axis and is given by:

$$\boldsymbol{C}_{bv_1}(-\delta_1) = \begin{bmatrix} \cos(-\delta_1) & 0 & \sin(-\delta_1) \\ 0 & 1 & 0 \\ -\sin(-\delta_1) & 0 & \cos(-\delta_1) \end{bmatrix} \tag{5.34}$$

The rotation matrix from the tip vane 2 frame to the spacecraft body frame, $\boldsymbol{C}_{bv_2}(\delta_1)$, is similar to the rotation matrix for tip vane 1, except the negative sign is removed from in

front of δ_1 since $\delta_2 = -\delta_1$.

$$\boldsymbol{C}_{bv_2}(\delta_1) = \begin{bmatrix} \cos(-\delta_2) & 0 & \sin(-\delta_2) \\ 0 & 1 & 0 \\ -\sin(-\delta_2) & 0 & \cos(-\delta_2) \end{bmatrix} = \begin{bmatrix} \cos(\delta_1) & 0 & \sin(\delta_1) \\ 0 & 1 & 0 \\ -\sin(\delta_1) & 0 & \cos(\delta_1) \end{bmatrix} \tag{5.35}$$

Once the moment of inertia matrices for each of these components with respect to the body frame are calculated, the parallel-axis and parallel-plane theorems must be used to calculate the diagonal and off-diagonal entries of the overall moment of inertia matrix, respectively. To use these theorems, it is necessary to know the positions of each component's mass center relative to the overall system mass center. These positions are determined using five vectors joining cm_t with the mass centers of each of these components and are defined as follows:

$$\boldsymbol{V}_p = \begin{bmatrix} V_{p,x} & V_{p,y} & V_{p,z} \end{bmatrix}^T = \begin{bmatrix} x_{cm_p} - x_{cm_t} & y_{cm_p} - y_{cm_t} & z_{cm_t} - z_{cm_p} \end{bmatrix}^T \tag{5.36}$$

$$\boldsymbol{V}_r = \begin{bmatrix} V_{r,x} & V_{r,y} & V_{r,z} \end{bmatrix}^T = \begin{bmatrix} x_{cm_r} - x_{cm_t} & y_{cm_r} - y_{cm_t} & z_{cm_t} - z_{cm_r} \end{bmatrix}^T \tag{5.37}$$

$$\boldsymbol{V}_s = \begin{bmatrix} V_{s,x} & V_{s,y} & V_{s,z} \end{bmatrix}^T = \begin{bmatrix} -x_{cm_t} & -y_{cm_t} & z_{cm_t} \end{bmatrix}^T \tag{5.38}$$

$$\boldsymbol{V}_{tv_1} = \begin{bmatrix} V_{tv_1,x} & V_{tv_1,y} & V_{tv_1,z} \end{bmatrix}^T = \begin{bmatrix} -x_{cm_t} & \left(\frac{a\sqrt{2}}{2} + \frac{2}{3}h\right) - y_{cm_t} & z_{cm_t} \end{bmatrix}^T \tag{5.39}$$

$$\boldsymbol{V}_{tv_2} = \begin{bmatrix} V_{tv_2,x} & V_{tv_2,y} & V_{tv_2,z} \end{bmatrix}^T = \begin{bmatrix} -x_{cm_t} & -\left(\frac{a\sqrt{2}}{2} + \frac{2}{3}h\right) - y_{cm_t} & z_{cm_t} \end{bmatrix}^T \tag{5.40}$$

These vectors are shown in Figure 5.5 and Figure 5.6.

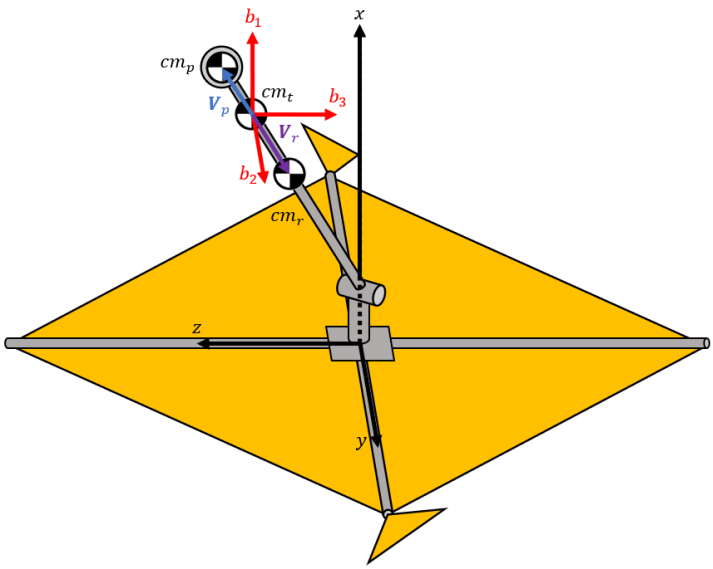

Figure 5.5: $\boldsymbol{V}_p$ and $\boldsymbol{V}_r$ Vectors used for Calculating $\boldsymbol{I}$

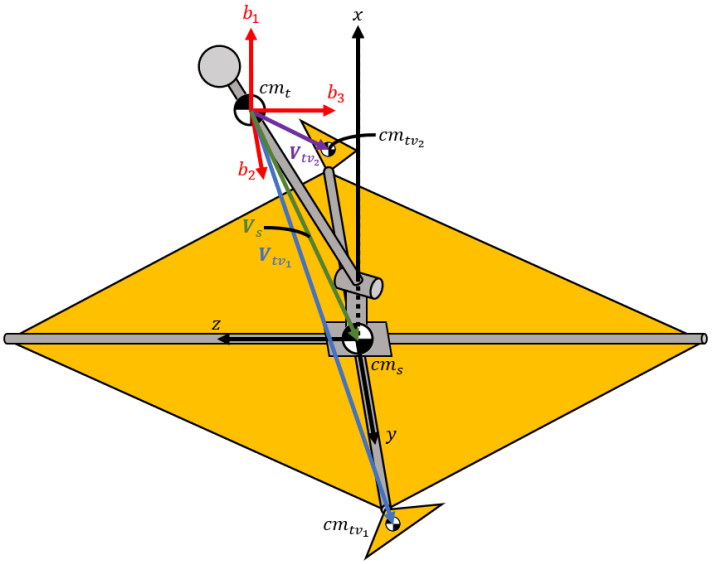

Figure 5.6: $\boldsymbol{V}_s$, $\boldsymbol{V}_{tv_1}$, and $\boldsymbol{V}_{tv_2}$ Vectors used for Calculating $\boldsymbol{I}$

Next, the components of the I_{11} entry of the overall moment of inertia matrix are calculated using the parallel-axis theorem as follows:

$$I_{11,p} = m_p \left(V_{p,y}^2 + V_{p,z}^2 \right) \tag{5.41}$$

$$I_{11,r} = I_{11,r,b} + m_r \left(V_{r,y}^2 + V_{r,z}^2\right) \tag{5.42}$$

$$I_{11,s} = I_{11,s,b} + m_s \left(V_{s,y}^2 + V_{s,z}^2\right) \tag{5.43}$$

$$I_{11,tv_1} = I_{11,tv_1,b} + m_{tv} \left(V_{tv_1,y}^2 + V_{tv_1,z}^2\right) \tag{5.44}$$

$$I_{11,tv_2} = I_{11,tv_2,b} + m_{tv} \left(V_{tv_2,y}^2 + V_{tv_2,z}^2\right) \tag{5.45}$$

Any variables with a b in the subscript indicate that these variables are entries in a component's moment of inertia matrix with respect to the spacecraft body frame

Next, the components of the I_{22} entry of the overall moment of inertia matrix are calculated using the parallel-axis theorem as follows:

$$I_{22,p} = m_p \left(V_{p,x}^2 + V_{p,z}^2\right) \tag{5.46}$$

$$I_{22,r} = I_{22,r,b} + m_r \left(V_{r,x}^2 + V_{r,z}^2\right) \tag{5.47}$$

$$I_{22,s} = I_{22,s,b} + m_s \left(V_{s,x}^2 + V_{s,z}^2\right) \tag{5.48}$$

$$I_{22,tv_1} = I_{22,tv_1,b} + m_{tv} \left(V_{tv_1,x}^2 + V_{tv_1,z}^2\right) \tag{5.49}$$

$$I_{22,tv_2} = I_{22,tv_2,b} + m_{tv} \left(V_{tv_2,x}^2 + V_{tv_2,z}^2\right) \tag{5.50}$$

Next, the components of the I_{33} entry of the overall moment of inertia matrix are calculated using the parallel-axis theorem as follows:

$$I_{33,p} = m_p \left(V_{p,x}^2 + V_{p,y}^2\right) \tag{5.51}$$

$$I_{33,r} = I_{33,r,b} + m_r \left(V_{r,x}^2 + V_{r,y}^2\right) \tag{5.52}$$

$$I_{33,s} = I_{33,s,b} + m_s \left(V_{s,x}^2 + V_{s,y}^2\right) \tag{5.53}$$

$$I_{33,tv_1} = I_{33,tv_1,b} + m_{tv} \left(V_{tv_1,x}^2 + V_{tv_1,y}^2\right) \tag{5.54}$$

$$I_{33,tv_2} = I_{33,tv_2,b} + m_{tv}\left(V_{tv_2,x}^2 + V_{tv_2,y}^2\right) \tag{5.55}$$

Next, the components of the I_{12} entry of the overall moment of inertia matrix are calculated using the parallel-plane theorem as follows:

$$I_{12,p} = m_p V_{p,x} V_{p,y} \tag{5.56}$$

$$I_{12,r} = I_{12,r,b} + m_r V_{r,x} V_{r,y} \tag{5.57}$$

$$I_{12,s} = I_{12,r,b} + m_s V_{s,x} V_{s,y} \tag{5.58}$$

$$I_{12,tv_1} = I_{12,tv_1,b} + m_{tv} V_{s,x} V_{s,y} \tag{5.59}$$

$$I_{12,tv_2} = I_{12,tv_2,b} + m_{tv} V_{s,x} V_{s,y} \tag{5.60}$$

Next, the components of the I_{23} entry of the overall moment of inertia matrix are calculated using the parallel-plane theorem as follows:

$$I_{23,p} = m_p V_{p,y} V_{p,z} \tag{5.61}$$

$$I_{23,r} = I_{23,r,b} + m_r V_{r,y} V_{r,z} \tag{5.62}$$

$$I_{23,s} = I_{23,r,b} + m_s V_{s,y} V_{s,z} \tag{5.63}$$

$$I_{23,tv_1} = I_{23,tv_1,b} + m_{tv} V_{s,y} V_{s,z} \tag{5.64}$$

$$I_{23,tv_2} = I_{23,tv_2,b} + m_{tv} V_{s,y} V_{s,z} \tag{5.65}$$

Next, the components of the I_{13} entry of the overall moment of inertia matrix are calculated using the parallel-plane theorem as follows:

$$I_{13,p} = m_p V_{p,x} V_{p,z} \tag{5.66}$$

$$I_{13,r} = I_{13,r,b} + m_r V_{r,x} V_{r,z} \tag{5.67}$$

$$I_{13,s} = I_{13,r,b} + m_s V_{s,x} V_{s,z} \tag{5.68}$$

$$I_{13,tv_1} = I_{13,tv_1,b} + m_{tv} V_{s,x} V_{s,z} \tag{5.69}$$

$$I_{13,tv_2} = I_{13,tv_2,b} + m_{tv} V_{s,x} V_{s,z} \tag{5.70}$$

Finally, the overall moment of inertia matrix is calculated by summing the contributions from the payload, rod, sail, and tip vanes:

$$I_{11} = I_{11,p} + I_{11,r} + I_{11,s} + I_{11,tv1} + I_{11,tv2} \tag{5.71}$$

$$I_{22} = I_{22,p} + I_{22,r} + I_{22,s} + I_{22,tv1} + I_{22,tv2} \tag{5.72}$$

$$I_{33} = I_{33,p} + I_{33,r} + I_{33,s} + I_{33,tv1} + I_{33,tv2} \tag{5.73}$$

$$I_{12} = I_{21} = I_{12,p} + I_{12,r} + I_{12,s} + I_{12,tv_1} + I_{12,tv_2} \tag{5.74}$$

$$I_{23} = I_{32} = I_{23,p} + I_{23,r} + I_{23,s} + I_{23,tv_1} + I_{23,tv_2} \tag{5.75}$$

$$I_{13} = I_{31} = I_{13,p} + I_{13,r} + I_{13,s} + I_{13,tv_1} + I_{13,tv_2} \tag{5.76}$$

$$\boldsymbol{I} = \begin{bmatrix} I_{11} & I_{12} & I_{13} \\ I_{12} & I_{22} & I_{23} \\ I_{13} & I_{23} & I_{33} \end{bmatrix} \tag{5.77}$$

5.7 Actuator Dynamics

A real-world motor cannot be commanded to move to a new angle instantaneously, since there are internal dynamics that result in a time delay between when a motor receives a command and when it rotates to a desired angle. To accurately model the dynamic response of the solar sail to changes in the gimballed payload position and tip vane orientation, the dynamics of the DC motors driving the gimbal mechanism and tip vanes must be incorporated into the simulation. For this thesis, the motors were assumed to behave like second-order systems

with the following transfer function in the frequency domain:

$$\frac{U_{act}(s)}{U_{com}(s)} = \frac{\omega_n^2}{s^2 + 2\zeta\omega_n s + \omega_n^2} \tag{5.78}$$

where $U_{com}(s)$ is the commanded motor angle (ϕ_g, θ_g, or δ_1), $U_{act}(s)$ is the actual value of the motor angle after it has begun moving to the commanded angle, ζ is the damping ratio, and ω_n is the natural frequency. ζ is chosen to be 1 for critical damping and a desired settling time, t_s, of 4 seconds was chosen for this system. The system's settling time, assuming it is achieved when the response is within $\pm 2\%$ of the input, can be calculated as follows [31]:

$$t_s = \frac{4}{\zeta\omega_n} \tag{5.79}$$

Using Equation (5.79), the system's natural frequency was determined to be 1 rad/s.

Taking the inverse Laplace transform of Equation (5.35) with $\zeta = 1$ yields the following second-order ODE:

$$\ddot{u}_{act} + 2\omega_n\dot{u}_{act} + \omega_n^2 u_{act} = \omega_n^2 u_{com} \tag{5.80}$$

After the gimballed rod is commanded to move to a new position and the tip vanes are commanded to a new orientation, Equation (5.80) is numerically integrated to obtain a value of u_{act} at each time step. To numerically integrate this equation, the variables u_1 and u_2 are defined to decompose the second-order ODE into a system of two first-order ODEs:

$$u_1 = u_{act} \tag{5.81}$$

$$u_2 = \dot{u}_{act} = \dot{u}_1 \tag{5.82}$$

Thus, the resulting system of differential equations is

$$\begin{bmatrix} \dot{u}_1 \\ \dot{u}_2 \end{bmatrix} = \begin{bmatrix} u_2 \\ -2\omega_n u_2 - \omega_n^2 u_1 + \omega_n^2 u_{com} \end{bmatrix} \tag{5.83}$$

which has the following initial conditions:

$$u_{1,0}(i) = u_{act,0}(i) = u_a ct(i-1) \tag{5.84}$$

$$u_{2,0}(i) = \dot{u}_{act,0}(i) = \dot{u}_a ct(i-1) \tag{5.85}$$

where i is the index representing the current time step (starting at $i = 1$). Equation (5.84) states that the next initial motor angle to be used for integrating ahead one time step is equal to the motor angle obtained from integrating in the previous time step. The same is true for the motor angle rate in Equation (5.85). At time $t = 0$, both initial conditions are zero.

The exact solution to Equation (5.80) is

$$u_{act} = u_{com} - e^{-\omega_n t}\left(1 + \omega_n t\right) \tag{5.86}$$

If u_{com} has a value of 1, then the response, u_{act}, will look like the curve shown in Figure 5.7.

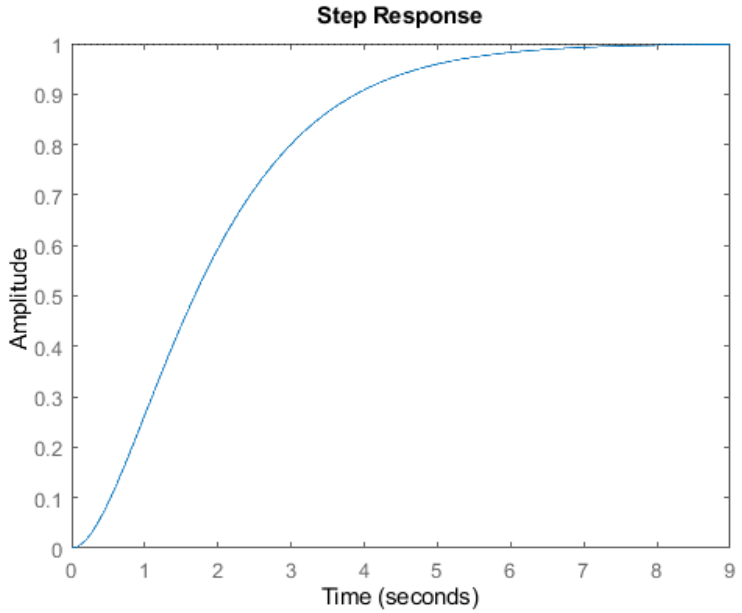

Figure 5.7: Motor Angle Response to a Unit-Step Input at $t = 0$ (Note: $\zeta = \omega_n = 1$)

From Equation (5.86) and Figure 5.7, it is evident that u_{act} will approach u_{com} asymptotically as $t \to \infty$. To account for this, a tolerance range of $\pm 2\%$ is created around the commanded motor angle for each time step of the simulation. If the actual motor angle comes within $\pm 2\%$ of the commanded motor angle, then the motors are considered to have reached their desired position. A range of $\pm 2\%$ was selected since it is a commonly used range for the settling time of second-order systems [31].

As a result of the motors being unable to rotate to their commanded angle instantaneously, the gimballed payload will generate intermediate torques as the motor rotates to its new angle. This was incorporated into the simulation and will be discussed in Section 5.8.

5.8 Simulation Procedure

The attitude control system was simulated in MATLAB using the fourth order Runge-Kutta method. All simulations used a fixed time step of 0.1 seconds. Two types of simulations were performed, one that does not consider actuator dynamics and one that does.

5.8.1 No Actuator Dynamics Incorporated

First, the desired Euler angles are converted to desired quaternion elements, $\boldsymbol{\epsilon}_d$, using MATLAB's angle2quat function. Next, the vector part of the error quaternion, $\boldsymbol{\epsilon}_e$, is calculated using Equation (5.3). Next, the desired control torques, $T_{b_1,d}$, $T_{b_2,d}$, and $T_{b_3,d}$, are calculated using Equation (5.2). Next, the gimbal angles needed to produce these torques are calculated using Equation (5.12) and Equation (5.13). Once the desired gimbal angles have been calculated, they are used to calculate the new spacecraft center of mass location. Next, the desired tip vane angles are calculated using moment arms taken with respect to the new center of mass location. Next, the actual control torques are calculated by summing the torque contributions from the gimballed payload and the tip vanes. If $\hat{\boldsymbol{s}}_b < 0$, then all the actual control torques are set to zero since the emissive sides of the sail and tip vanes are facing the Sun and cannot produce any torques. Next, the new moment of inertia matrix is

calculated using (5.77) as well as its inverse, then (5.4) and Equation (5.5) are numerically integrated ahead one time step to obtain new $\boldsymbol{\omega}$ and $\boldsymbol{\epsilon}$ vectors, and the "Simulate Spacecraft Dynamics" block shown in Figure 5.8 is exited. The $\boldsymbol{\omega}$ and $\boldsymbol{\epsilon}$ vectors are used to compute new $\boldsymbol{\epsilon}_e$, $\hat{\boldsymbol{s}}_b$, and $\boldsymbol{T}_{c,d}$ vectors. This loop continues until the end of the pre-defined analysis duration. When the simulation is finished, the quaternion elements are converted to Euler angles using MATLAB's quat2angle function for visualisation purposes.

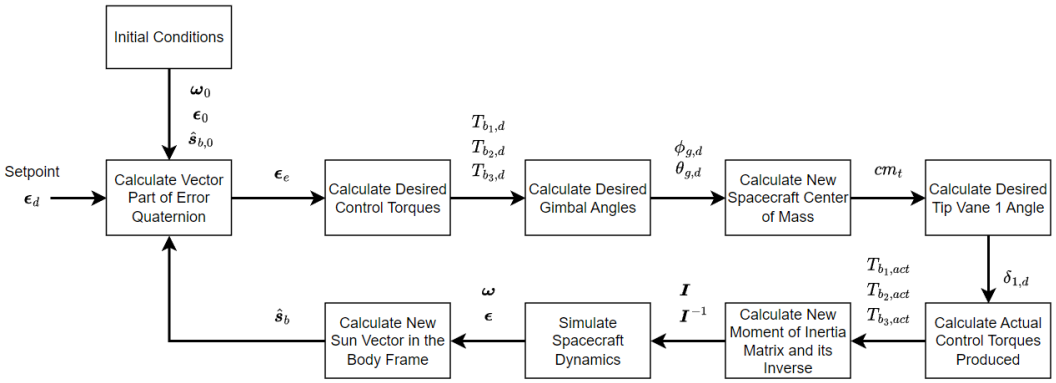

Figure 5.8: Attitude Control Simulation Diagram without Actuator Dynamics

5.8.2 Actuator Dynamics Incorporated

In this case, $\boldsymbol{\epsilon}_d$, $\boldsymbol{\epsilon}_e$, $\boldsymbol{T}_{c,d}$, and the desired gimbal and tip vane angles are calculated using the same equations as the "no actuator dynamics incorporated" case. If the current gimbal and tip vane angles, which are initially zero at $t = 0$, are within $\pm 2\%$ of the desired angles, then the gimbal and tip vane angles remain the same and the actual control torques exerted on the solar sail are the same as they were in the previous time step. Like the "no actuator dynamics" case, if $\hat{\boldsymbol{s}}_b < 0$, then all of the actual control torques are set to zero. Next, Equation (5.4) and Equation (5.5) are numerically integrated ahead one time step to obtain new $\boldsymbol{\omega}$ and $\boldsymbol{\epsilon}$ vectors, then a new $\hat{\boldsymbol{s}}_b$ vector is calculated and the Dynamics Block shown in Figure 5.9 and Figure 5.10 is exited. The $\boldsymbol{\omega}$ and $\boldsymbol{\epsilon}$ vectors are used to compute a new $\boldsymbol{\epsilon}_e$ vector and desired control torques $T_{b_2,d}$ and $T_{b_3,d}$.

If none of the gimbal and tip vane angles are within ±2% of the desired angles, the effect of actuator dynamics is simulated by numerically integrating the system of ODEs in Equation (5.83) ahead one time step. The system of ODEs is only numerically integrated for the gimbal and tip vane angles that are not within 2% of the desired angles. If any of the gimbal and tip vane angles are within this range, then its value remains the same from the previous time step and the corresponding angle rate is set to 0 deg/s. The current gimbal and tip vane angles and the current $\hat{\boldsymbol{s}}_b$ vector are used to calculate actual torques generated by the gimballed payload and tip vanes. Next, the new moment of inertia matrix is calculated using Equation (5.77) as well as its inverse. Lastly, Equation (5.4) and Equation (5.5) are numerically integrated ahead one time step and the loop continues until all gimbal and tip vane angles are within ±2% of the desired angles, at which point the Dynamics Block is exited. The final $\boldsymbol{\omega}$ and $\boldsymbol{\epsilon}$ vectors produced by this numerical integration are used to compute new $\boldsymbol{\epsilon}_e$, $\hat{\boldsymbol{s}}_b$, and $\boldsymbol{T}_{c,d}$ vectors. Like the "no actuator dynamics" case, the quaternion elements are converted to Euler angles for visualisation purposes once the simulation is complete.

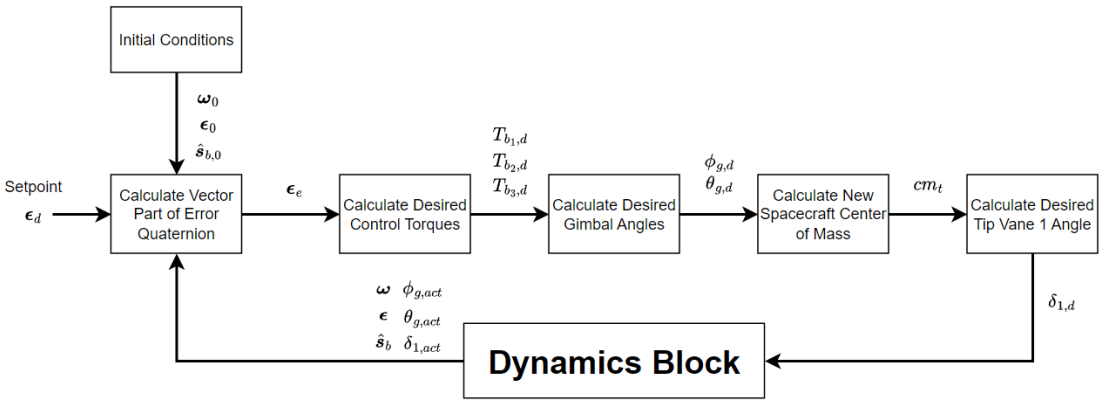

Figure 5.9: Attitude Control Simulation Diagram with Actuator Dynamics

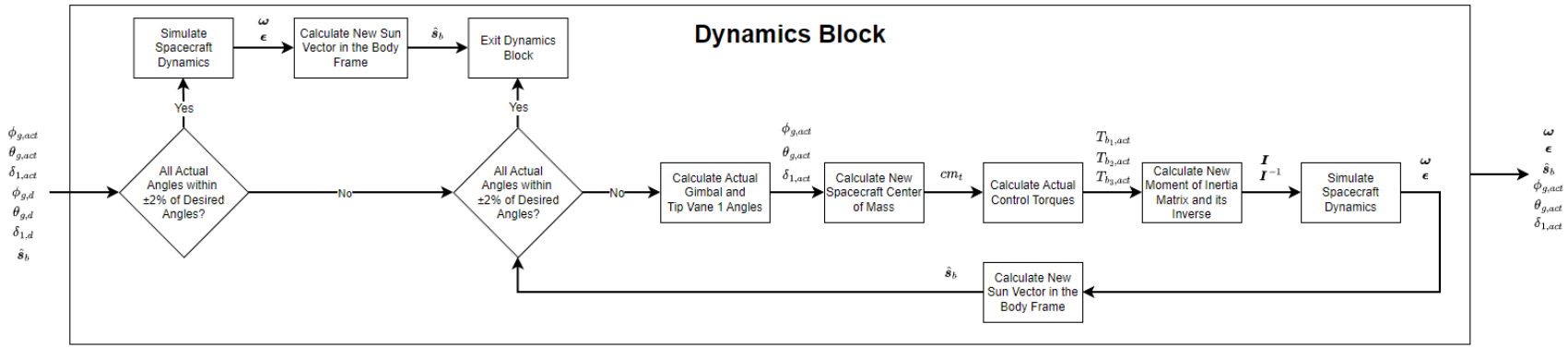

Figure 5.10: Dynamics Block

6 Phase 1 Simulation Results

For Phase 1, the solar sail model discussed in Section 5 was simulated without tip vanes under a range of initial conditions with varying attitude setpoints to assess the performance of the gimballed mass quaternion-based PD control scheme. For plots comparing results obtained with and without actuator dynamics, "NAD" refers to "no actuator dynamics" and "AD" refers to "actuator dynamics." Unless otherwise specified, the natural frequency of the gimbal mechanism's motors, ω_n, is equal to 1 rad/s. The Phase 1 simulation results are examined in the following sections.

6.1 Non-Zero Initial Angular Velocities and Zero Desired Attitude

In the following two cases, the sail was commanded to a zero attitude with varying initial angular velocities and a constant initial attitude of $[\theta_1, \theta_2, \theta_3] = [0°, 10°, 10°]$.

6.1.1 Case 1 Results

In this case, the initial conditions $[\omega_1, \omega_2, \omega_3] = [0, 5, 5] \times 10^{-4}$ rad/s and $[\theta_1, \theta_2, \theta_3] = [0°, 10°, 10°]$ were used.

In Figure 6.1, ω_2 and ω_3 converge to 0 deg/s in approximately eight hours, while the roll axis angular velocity ω_1, which is uncontrolled, initially fluctuates for a period of four hours before stabilizing. As shown in Figure 6.3, all angular velocities between the "no actuator dynamics" and "actuator dynamics" cases follow each other quite closely, with the absolute value of the largest differences being on the order of 1×10^{-5} deg/s. Similar behaviour is also observed for the Euler angles, with the largest difference being approximately 0.9° for the roll axis angle at steady state. As shown in Equation (5.4) and Equation (5.5), some coupling exists between the equations of motion, so this induced motion about the roll axis is to be expected.

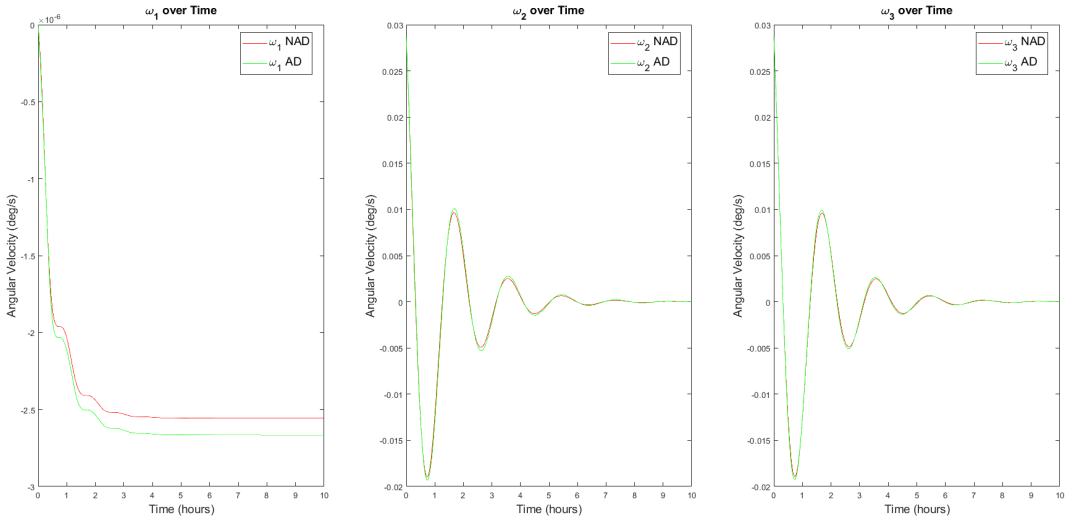

Figure 6.1: Angular Velocities with Setpoint $[\theta_1, \theta_2, \theta_3] = [0°, 0°, 0°]$ and Initial Conditions $[\omega_1, \omega_2, \omega_3] = [0, 5, 5] \times 10^{-4}$ rad/s and $[\theta_1, \theta_2, \theta_3] = [0°, 10°, 10°]$

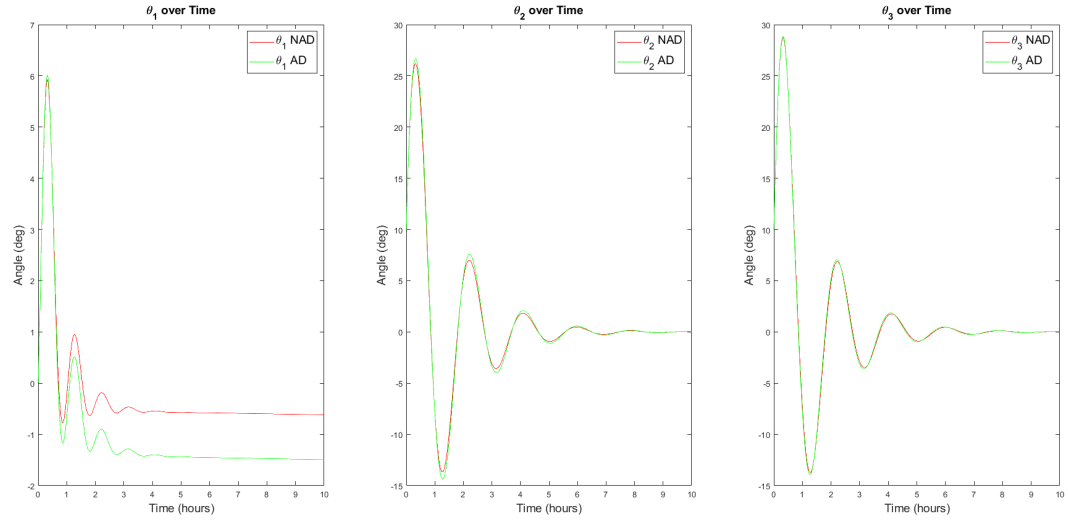

Figure 6.2: Euler Angles with Setpoint $[\theta_1, \theta_2, \theta_3] = [0°, 0°, 0°]$ and Initial Conditions $[\omega_1, \omega_2, \omega_3] = [0, 5, 5] \times 10^{-4}$ rad/s and $[\theta_1, \theta_2, \theta_3] = [0°, 10°, 10°]$

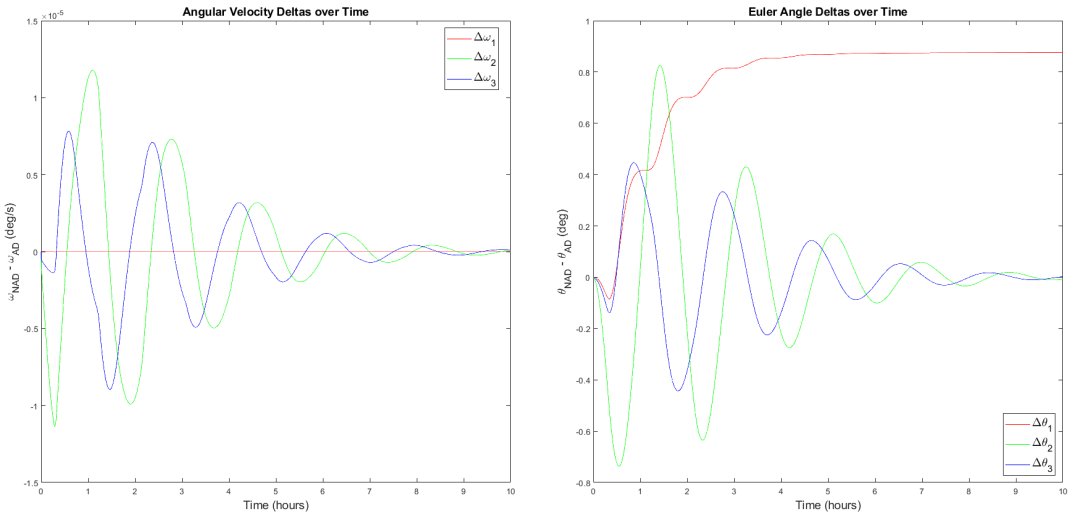

Figure 6.3: Angular Velocity and Euler Angle Deltas with Setpoint $[\theta_1, \theta_2, \theta_3] = [0°, 0°, 0°]$ and Initial Conditions $[\omega_1, \omega_2, \omega_3] = [0, 5, 5] \times 10^{-4}$ rad/s and $[\theta_1, \theta_2, \theta_3] = [0°, 10°, 10°]$

Time histories of the actual control torques were also obtained and can be found in Figure 6.4. The largest differences between the control torques were on the order of -19.6×10^{-4} Nm, so much like the angular velocities and Euler angles, the "no actuator dynamics" and "actuator dynamics" control torques also follow each other quite closely.

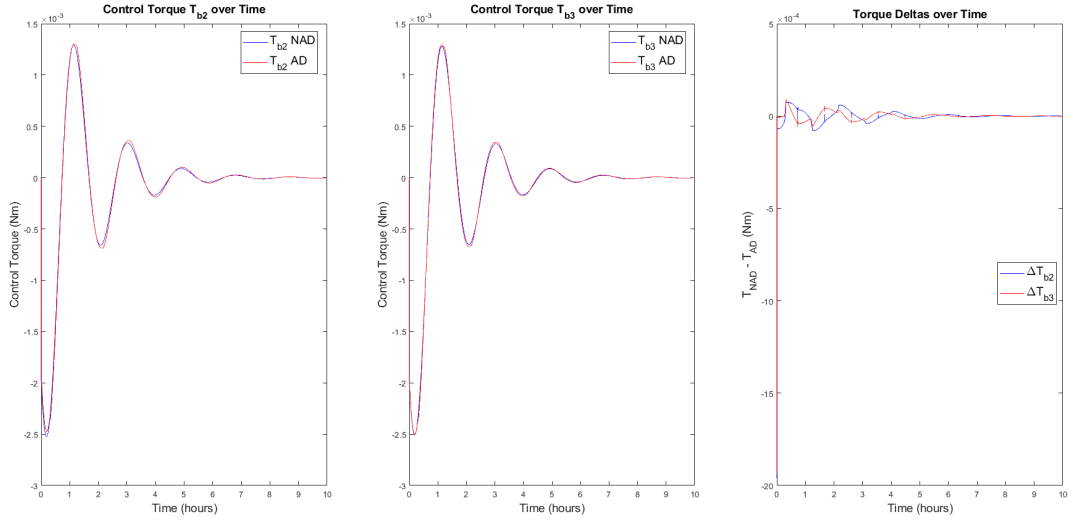

Figure 6.4: Control Torques with Setpoint $[\theta_1, \theta_2, \theta_3] = [0°, 0°, 0°]$ and Initial Conditions $[\omega_1, \omega_2, \omega_3] = [0, 5, 5] \times 10^{-4}$ rad/s and $[\theta_1, \theta_2, \theta_3] = [0°, 10°, 10°]$

Time histories of the actual gimbal clock and cone angles are shown in Figure 6.5. The gimbal clock angles follow each other closely but begin to diverge from each other after approximately 30 minutes. At 45 minutes, both clock angles undergo a rapid oscillation between +90° and -90°. This rapid change occurs nine more times at 1-hour intervals. The cone angles achieve a maximum value of approximately -18.5° after 15 minutes and eventually converge to 0° after eight hours.

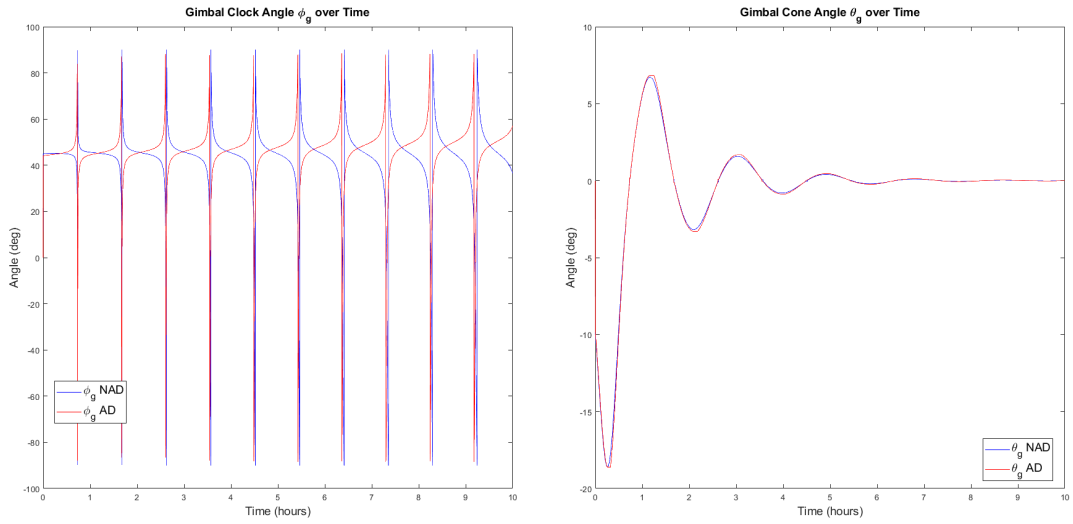

Figure 6.5: Gimbal Angles with Setpoint $[\theta_1, \theta_2, \theta_3] = [0°, 0°, 0°]$ and Initial Conditions $[\omega_1, \omega_2, \omega_3] = [0, 5, 5] \times 10^{-4}$ rad/s and $[\theta_1, \theta_2, \theta_3] = [0°, 10°, 10°]$

6.1.2 Case 2 Results

In this case, the initial conditions $[\omega_1, \omega_2, \omega_3] = [0, 5, 5] \times 10^{-3}$ rad/s and $[\theta_1, \theta_2, \theta_3] = [0°, 10°, 10°]$ were used. ω_n has also been set to 6 rad/s for this simulation, which corresponds to a settling time of approximately 0.67 s. This is the lowest natural frequency that allows the "actuator dynamics" results to settle within a ten-hour period.

Note that the initial angular velocities have been increased by one order of magnitude. As shown in Figure 6.6, there is a larger discrepancy between the "no actuator dynamics" and "actuator dynamics" angular velocities and they both take about two hours longer to achieve steady state than the previous case with smaller initial angular velocities. The Euler angles

in Figure 6.7 are problematic since some of the attitudes in the first five hours indicate that the sail's radiator has rotated to face the Sun, which complicates temperature regulation.

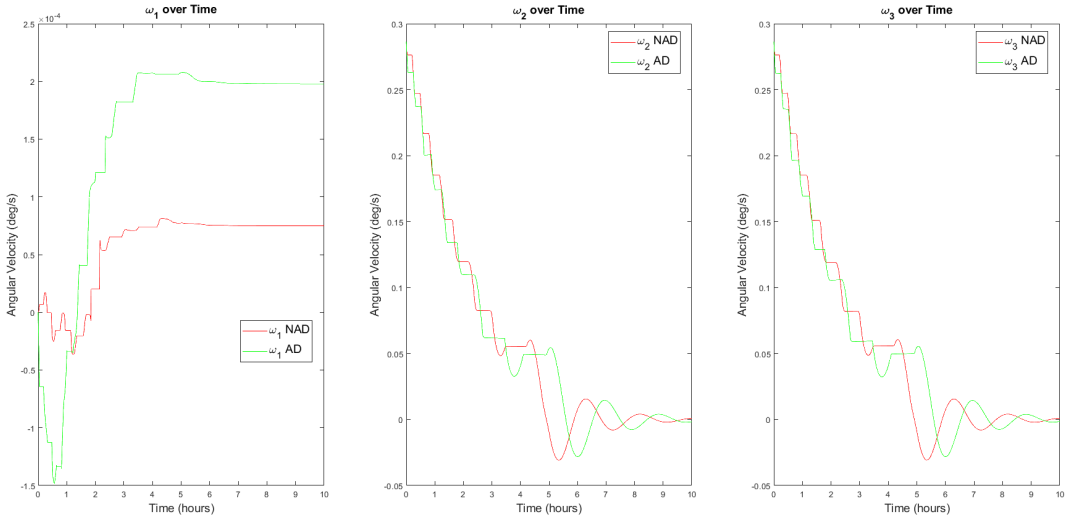

Figure 6.6: Angular Velocities with Setpoint $[\theta_1, \theta_2, \theta_3] = [0°, 0°, 0°]$ and Initial Conditions $[\omega_1, \omega_2, \omega_3] = [0, 5, 5] \times 10^{-3}$ rad/s and $[\theta_1, \theta_2, \theta_3] = [0°, 10°, 10°]$

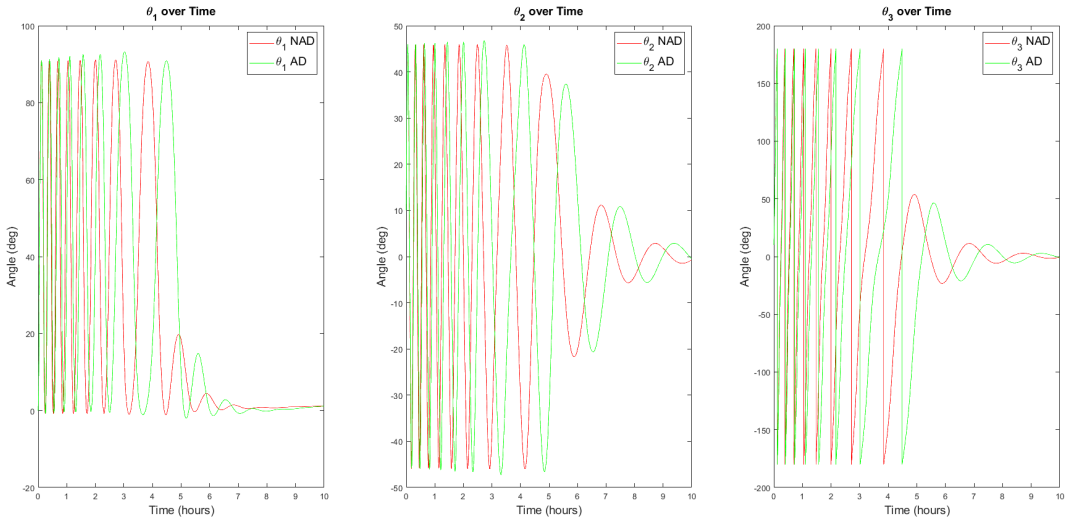

Figure 6.7: Euler Angles with Setpoint $[\theta_1, \theta_2, \theta_3] = [0°, 0°, 0°]$ and Initial Conditions $[\omega_1, \omega_2, \omega_3] = [0, 5, 5] \times 10^{-3}$ rad/s and $[\theta_1, \theta_2, \theta_3] = [0°, 10°, 10°]$

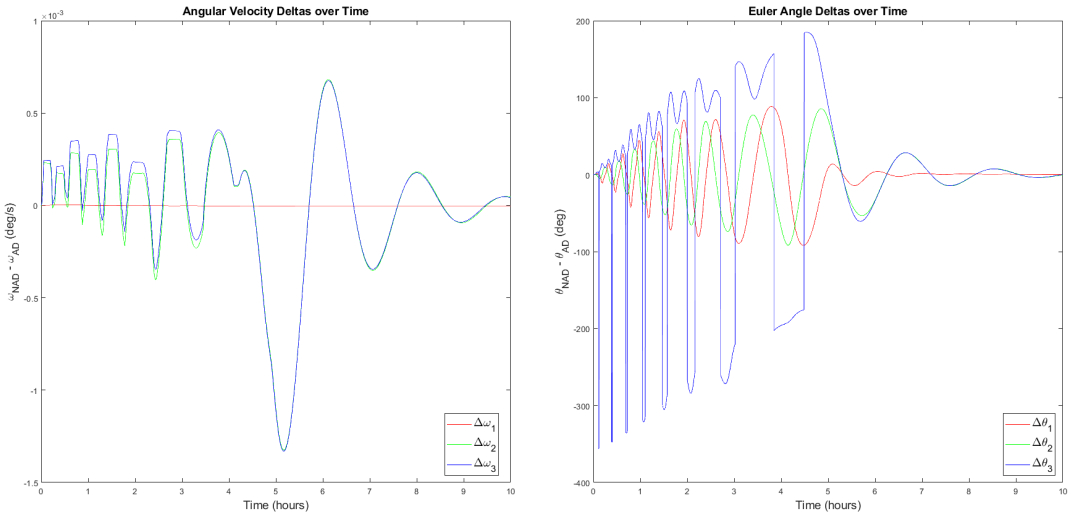

Figure 6.8: Angular Velocity and Euler Angle Deltas with Setpoint $[\theta_1, \theta_2, \theta_3] = [0°, 0°, 0°]$ and Initial Conditions $[\omega_1, \omega_2, \omega_3] = [0, 5, 5] \times 10^{-3}$ rad/s and $[\theta_1, \theta_2, \theta_3] = [0°, 10°, 10°]$

6.2 Zero Initial Angular Velocities and Non-Zero Desired Attitude

In the following two cases, the sail was commanded to the non-zero attitude $[\theta_1, \theta_2, \theta_3] = [0°, 20°, 20°]$ with zero initial angular velocities and varying initial attitudes.

6.2.1 Case 1 Results

In this case, the initial conditions $[\omega_1, \omega_2, \omega_3] = [0, 0, 0]$ rad/s and $[\theta_1, \theta_2, \theta_3] = [0°, 10°, 10°]$ were used.

It can be seen in Figure 6.9, that the ω_2 and ω_3 angular velocities between the "no actuator dynamics" and "actuator dynamics" cases follow each other quite closely. The absolute value of the largest difference between them is approximately 3.5×10^{-6} deg/s as shown in Figure 6.11. Like in Section 6.1, the ω_2 and ω_3 also reach steady state after about eight hours. The induced rotational motion about the roll axis is also observed with ω_1 plateauing after five hours for both the "no actuator dynamics" and "actuator dynamics" cases. In Figure 6.10, θ_2 and θ_3 initially oscillate about the setpoints but converge after about eight hours. The roll axis angle, θ_1, converges to approximately 2.5° at steady state.

This is more of a deviation from 0° compared to the roll axis angles in the prior two cases, but it is to be expected since no control torques are produced about this axis.

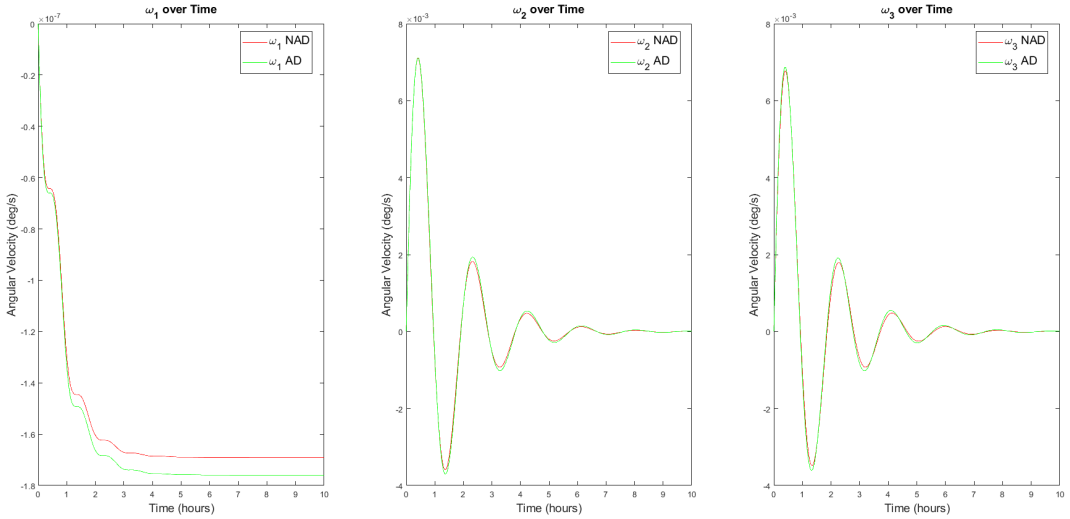

Figure 6.9: Angular Velocities with Setpoint $[\theta_1, \theta_2, \theta_3] = [0°, 20°, 20°]$ and Initial Conditions $[\omega_1, \omega_2, \omega_3] = [0, 0, 0]$ rad/s and $[\theta_1, \theta_2, \theta_3] = [0°, 10°, 10°]$

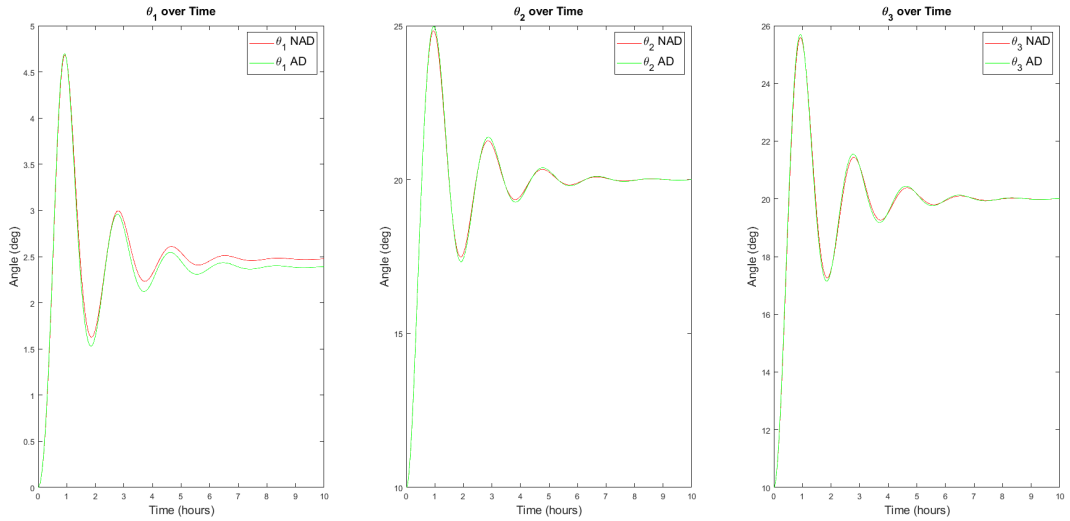

Figure 6.10: Euler Angles with Setpoint $[\theta_1, \theta_2, \theta_3] = [0°, 20°, 20°]$ and Initial Conditions $[\omega_1, \omega_2, \omega_3] = [0, 0, 0]$ rad/s and $[\theta_1, \theta_2, \theta_3] = [0°, 10°, 10°]$

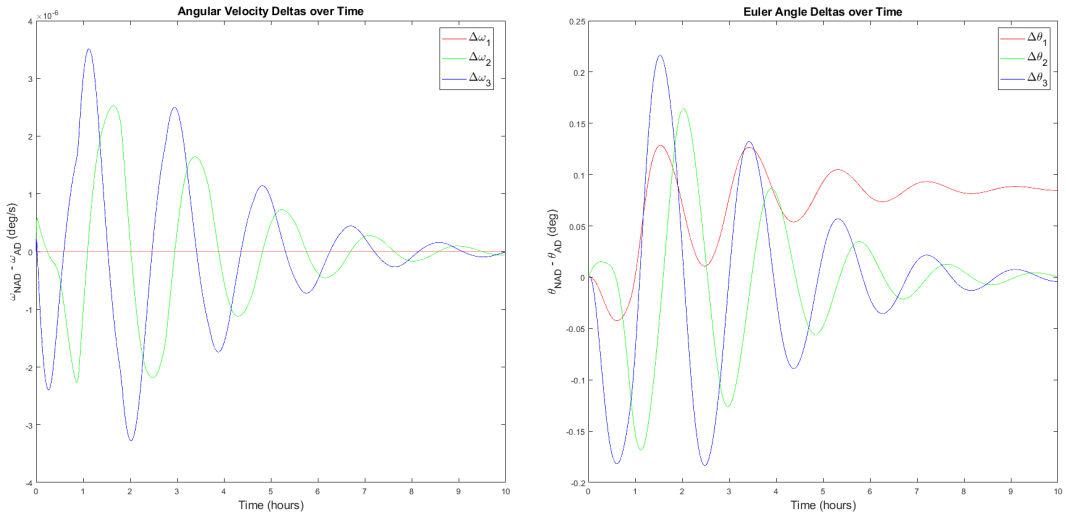

Figure 6.11: Angular Velocity and Euler Angle Deltas with Setpoint $[\theta_1, \theta_2, \theta_3] = [0°, 20°, 20°]$ and Initial Conditions $[\omega_1, \omega_2, \omega_3] = [0, 0, 0]$ rad/s and $[\theta_1, \theta_2, \theta_3] = [0°, 10°, 10°]$

Time histories of the actual control torques and gimbal angles are shown in Figure 6.12 and Figure 6.13, respectively. The largest difference between the actuator dynamics and "no actuator dynamics" control torques occurs close to the start of the simulation and is approximately 8.5×10^{-4} Nm for the b_2 axis torque. Initially, both gimbal clock angles in Figure 6.13 follow each other quite closely, but the "actuator dynamics" clock angle starts to lead the "no actuator dynamics" clock angle near the peaks at +90° and -90° as time goes on. The cone angles both reach a maximum of approximately 4° initially and later decay to 0° over time.

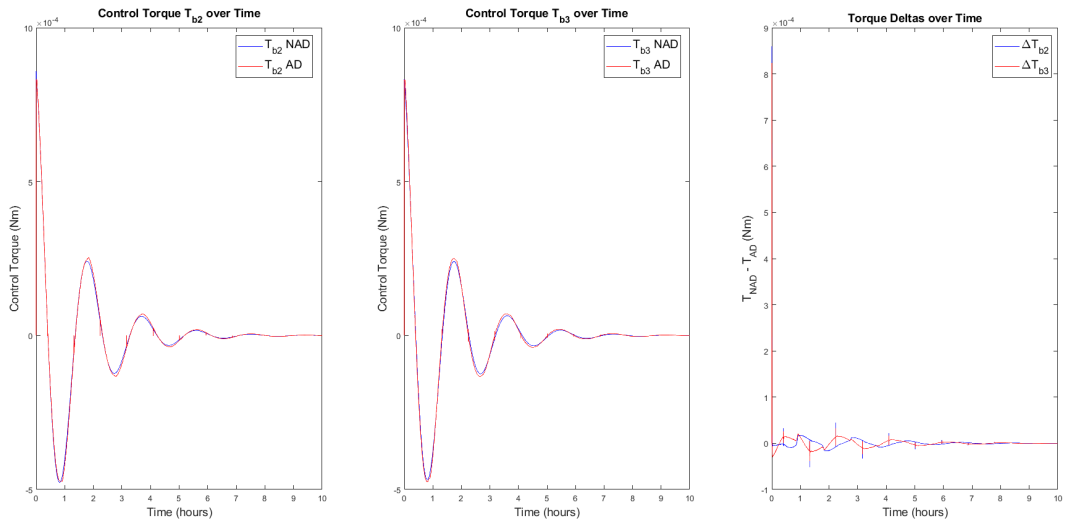

Figure 6.12: Control Torques with Setpoint $[\theta_1, \theta_2, \theta_3] = [0°, 20°, 20°]$ and Initial Conditions $[\omega_1, \omega_2, \omega_3] = [0, 0, 0]$ rad/s and $[\theta_1, \theta_2, \theta_3] = [0°, 10°, 10°]$

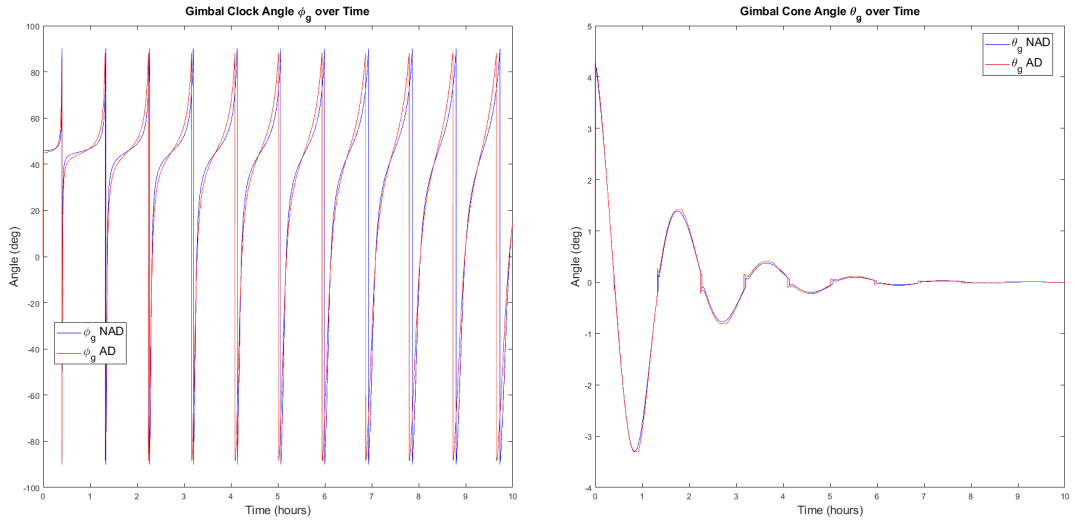

Figure 6.13: Gimbal Angles with Setpoint $[\theta_1, \theta_2, \theta_3] = [0°, 20°, 20°]$ and Initial Conditions $[\omega_1, \omega_2, \omega_3] = [0, 0, 0]$ rad/s and $[\theta_1, \theta_2, \theta_3] = [0°, 10°, 10°]$

6.2.2 Case 2 Results

In this case, the initial conditions $[\omega_1, \omega_2, \omega_3] = [0, 0, 0]$ rad/s and $[\theta_1, \theta_2, \theta_3] = [0°, 30°, 30°]$ were used.

As shown in Figure 6.16, there is little difference between the "no actuator dynamics"

and "actuator dynamics" angular velocities and Euler angles. The values of θ_1 in Figure 6.15 converges to approximately -4°after eight hours. Like the previous cases, since the current system does not possess control authority over the roll axis, θ_1 does not converge to 0°.

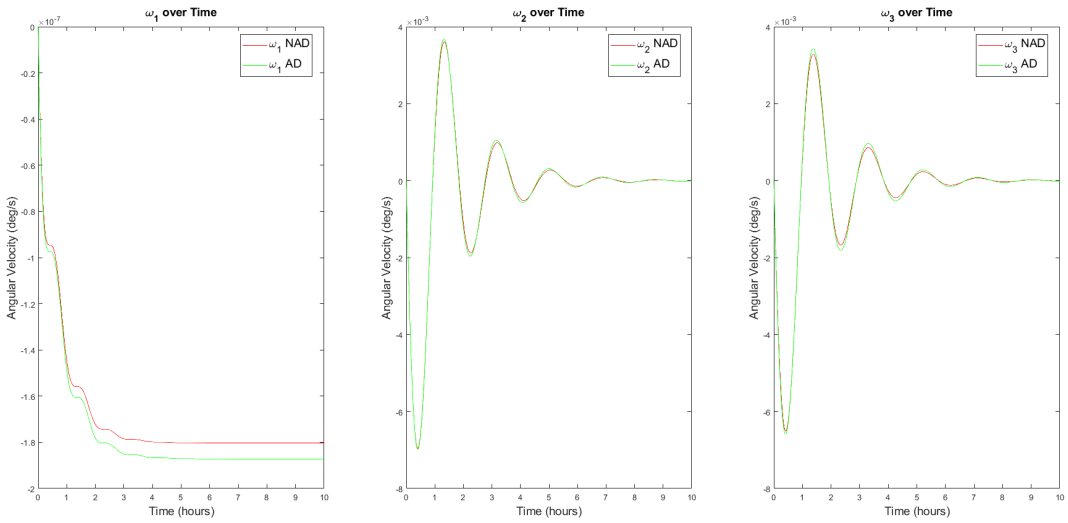

Figure 6.14: Angular Velocities with Setpoint $[\theta_1, \theta_2, \theta_3] = [0°, 20°, 20°]$ and Initial Conditions $[\omega_1, \omega_2, \omega_3] = [0, 0, 0]$ rad/s and $[\theta_1, \theta_2, \theta_3] = [0°, 30°, 30°]$

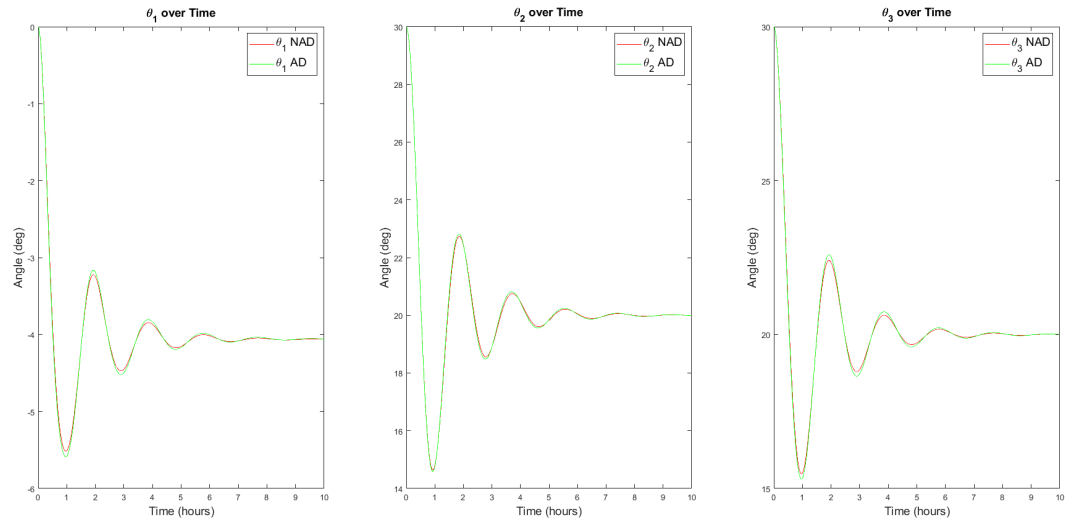

Figure 6.15: Euler Angles with Setpoint $[\theta_1, \theta_2, \theta_3] = [0°, 20°, 20°]$ and Initial Conditions $[\omega_1, \omega_2, \omega_3] = [0, 0, 0]$ rad/s and $[\theta_1, \theta_2, \theta_3] = [0°, 10°, 10°]$

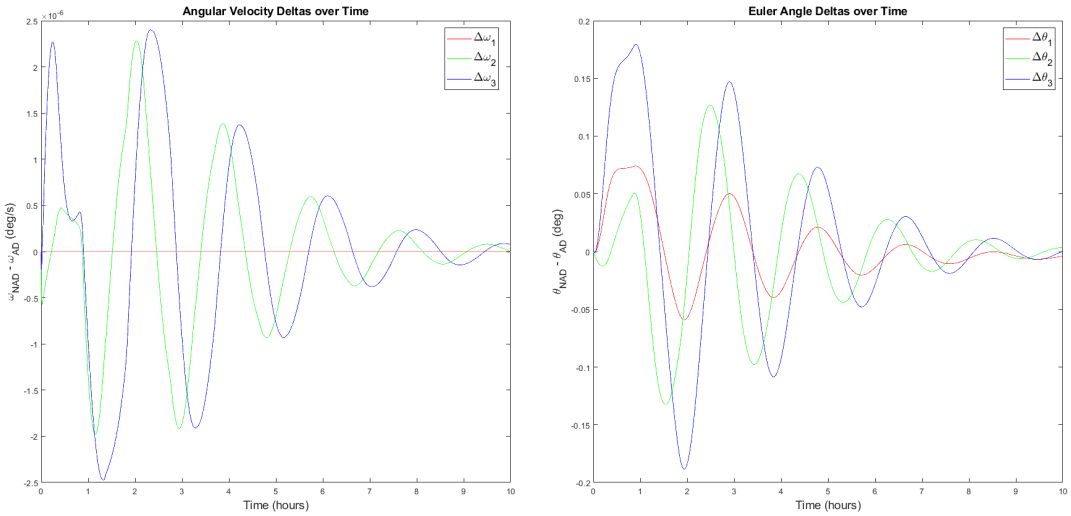

Figure 6.16: Angular Velocity and Euler Angle Deltas with Setpoint $[\theta_1, \theta_2, \theta_3] = [0°, 20°, 20°]$ and Initial Conditions $[\omega_1, \omega_2, \omega_3] = [0, 0, 0]$ rad/s and $[\theta_1, \theta_2, \theta_3] = [0°, 10°, 10°]$

6.3 Summary of Phase 1 Results

The results presented in this section indicate that the system converges within eight hours for most initial conditions and setpoints. It was observed in Section 6.1.2 that increasing the initial ω_2 and ω_3 angular velocities to 5×10^{-3} rad/s resulted in the system taking two hours longer to converge (although θ_2 was still experiencing some oscillation at the ten-hour mark). The larger initial ω_2 and ω_3 angular velocities also resulted in some concerning initial attitudes. Therefore, a limitation of this system is that larger initial angular velocities result in longer settling times. It was also observed for most cases that the inclusion of actuator dynamics does not result in significant differences between the "no actuator dynamics" and "actuator dynamics" angular velocities and Euler angles. However, if the initial angular velocities were on the order of 10^{-3} rad/s, then any value of ω_n less than 6 rad/s did not result in convergence for the "actuator dynamics" results. Therefore, it can be concluded that the settling time of the gimbal motors becomes critical to ensuring convergence as the initial angular velocities increase. The most significant difference was seen in Section 6.1.1

where the "no actuator dynamics" θ_1 angle was approximately 0.9° larger than the "actuator dynamics" θ_1 angle.

7 Phase 2 Simulation Results

For Phase 2, the solar sail model described in Section 5 was simulated under a range of initial conditions with varying attitude setpoints to assess the performance of the control scheme with the inclusion of tip vanes. As with Phase 1, Phase 2 also compared the system responses with and without actuator dynamics incorporated. Unless otherwise specified, the natural frequency of the gimbal mechanism's motors, ω_n, is equal to 1 rad/s. The Phase 2 simulation results are discussed in the following sections.

7.1 Non-Zero Initial Angular Velocities and Zero Desired Attitude

In the following two cases, the sail was commanded to a zero attitude with varying initial angular velocities and a constant initial attitude of $[\theta_1, \theta_2, \theta_3] = [10°, 10°, 10°]$.

7.1.1 Case 1 Results

In this case, the initial conditions $[\omega_1, \omega_2, \omega_3] = [5, 5, 5] \times 10^{-5}$ rad/s and $[\theta_1, \theta_2, \theta_3] = [10°, 10°, 10°]$ were used.

It can be observed in Figures 7.1 and 7.2 that ω_2, ω_3, θ_2, and θ_3 converge within eight hours, whereas ω_1 and θ_1 do not converge until after the ten-hour simulation duration. This is likely due to the relatively lower torques produced by the tip vanes in comparison to the gimballed payload.

Comparable to the Phase 1 results, the angular velocities and Euler angle results between the "no actuator dynamics" and "actuator dynamics" cases also follow each other closely, with the largest absolute value of the differences being 4×10^{-6} rad/s and 0.24°for the angular velocities and Euler angles, respectively.

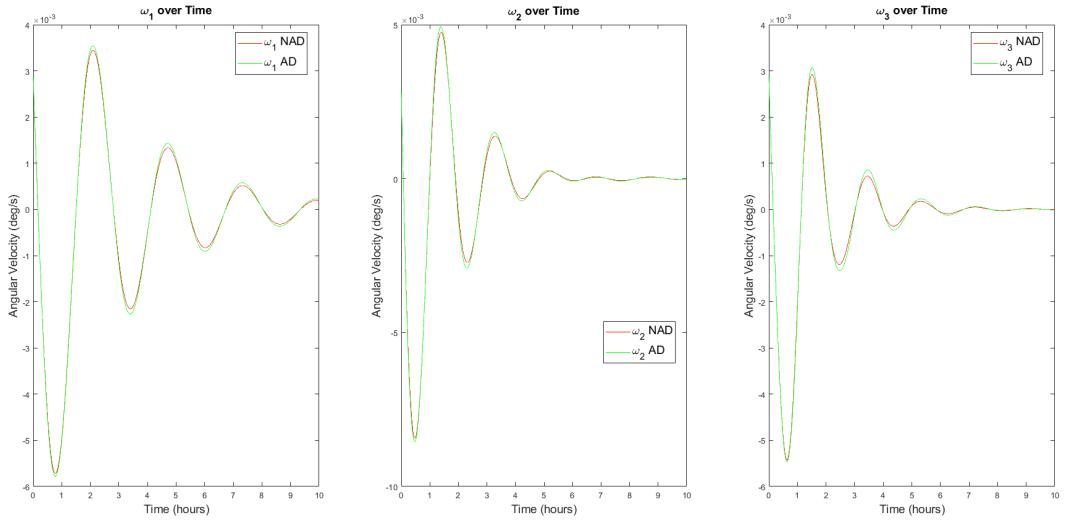

Figure 7.1: Angular Velocities with Setpoint $[\theta_1, \theta_2, \theta_3] = [0°, 0°, 0°]$ and Initial Conditions $[\omega_1, \omega_2, \omega_3] = [5, 5, 5] \times 10^{-5}$ rad/s and $[\theta_1, \theta_2, \theta_3] = [10°, 10°, 10°]$

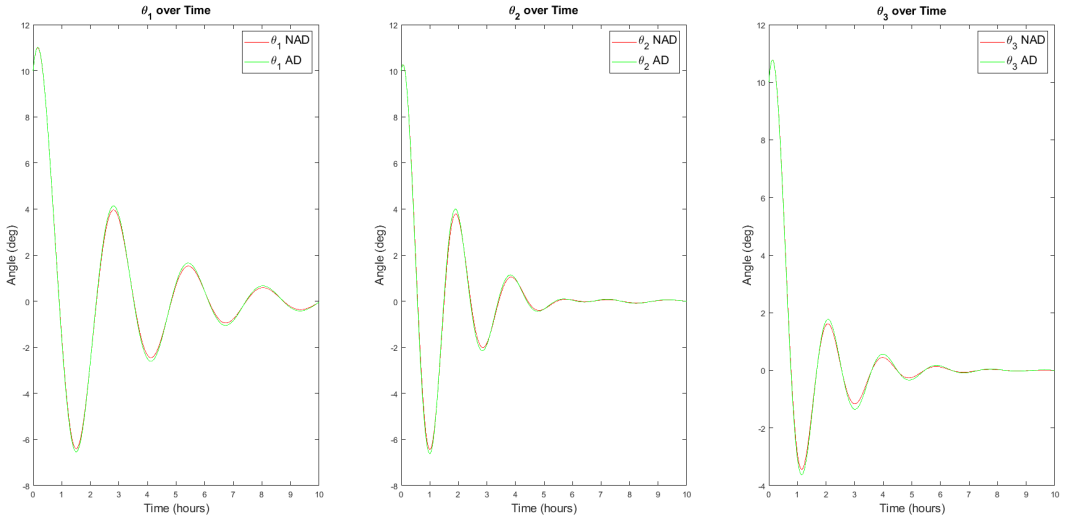

Figure 7.2: Euler Angles with Setpoint $[\theta_1, \theta_2, \theta_3] = [0°, 0°, 0°]$ and Initial Conditions $[\omega_1, \omega_2, \omega_3] = [5, 5, 5] \times 10^{-5}$ rad/s and $[\theta_1, \theta_2, \theta_3] = [10°, 10°, 10°]$

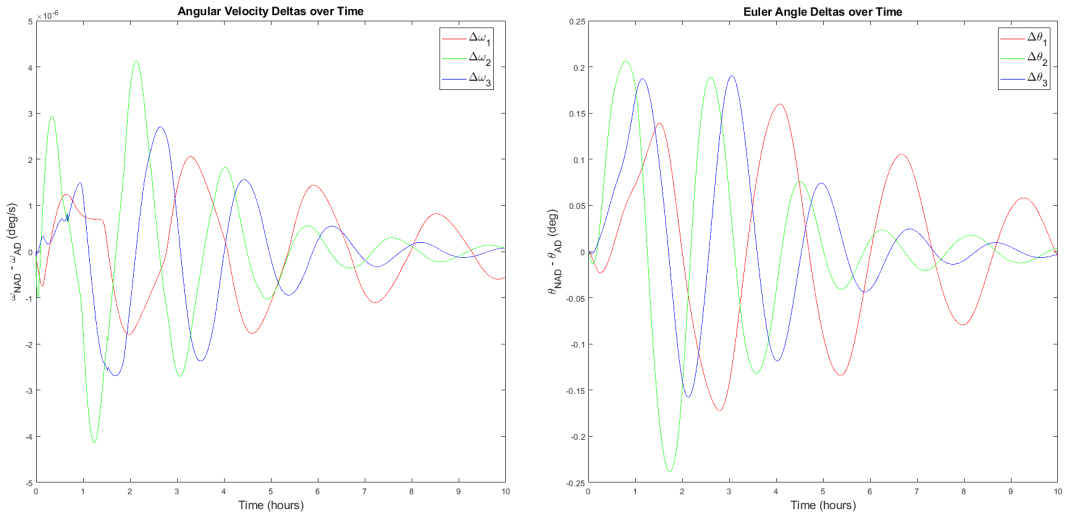

Figure 7.3: Angular Velocity and Euler Angle Deltas with Setpoint $[\theta_1, \theta_2, \theta_3] = [0°, 0°, 0°]$ and Initial Conditions $[\omega_1, \omega_2, \omega_3] = [5, 5, 5] \times 10^{-5}$ rad/s and $[\theta_1, \theta_2, \theta_3] = [10°, 10°, 10°]$

As can be seen in Figure 7.4, the gimballed payload produces larger torques about the b_2 and b_3 axes within the first four hours of the simulation compared to the tip vanes, thus resulting in faster convergence of the angular velocities and Euler angles.

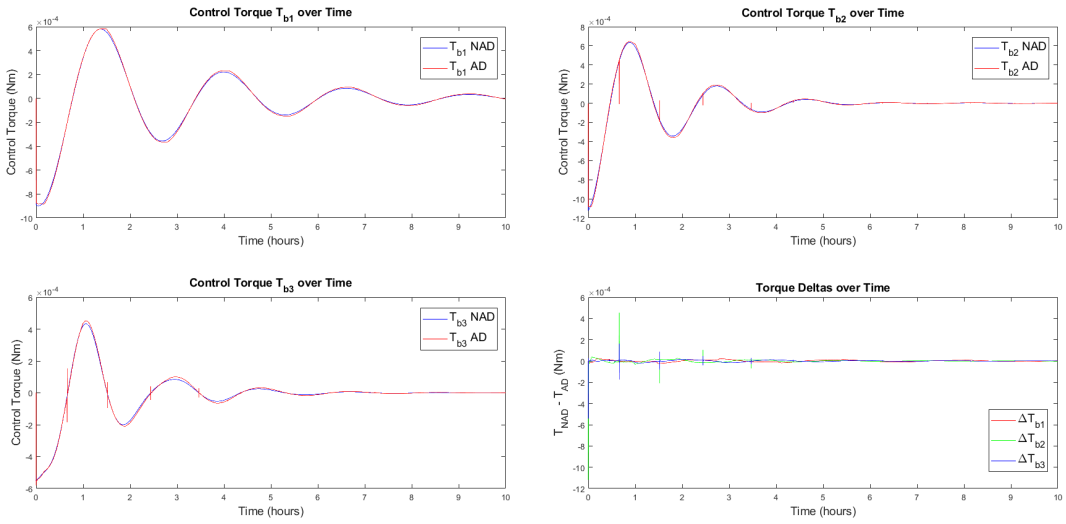

Figure 7.4: Control Torques with Setpoint $[\theta_1, \theta_2, \theta_3] = [0°, 0°, 0°]$ and Initial Conditions $[\omega_1, \omega_2, \omega_3] = [5, 5, 5] \times 10^{-5}$ rad/s and $[\theta_1, \theta_2, \theta_3] = [10°, 10°, 10°]$

Time histories of the gimbal and tip vane angles are shown in 7.5. Note that only the tip

vane 1 angle is plotted, since δ_2 would just be a mirror image of this plot. Both gimbal cone and tip vane angles converge towards 0°, with the cone angle experiencing faster convergence within eight hours. The absolute value of the cone and tip vane angles are relatively small compared to the clock angle, with the largest angles reaching approximately 5°initially.

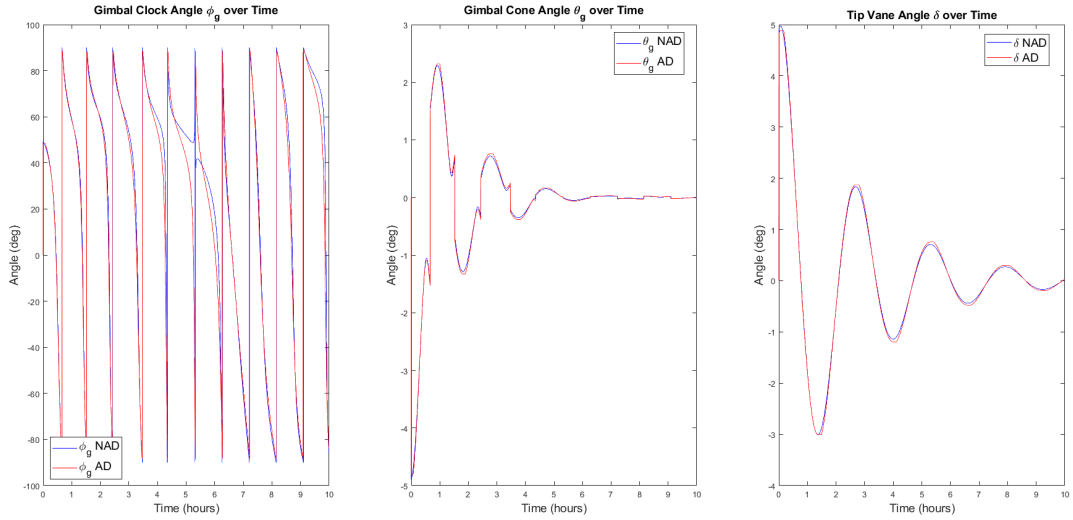

Figure 7.5: Gimbal and Tip Vane Angles with Setpoint $[\theta_1, \theta_2, \theta_3] = [0°, 0°, 0°]$ and Initial Conditions $[\omega_1, \omega_2, \omega_3] = [5, 5, 5] \times 10^{-5}$ rad/s and $[\theta_1, \theta_2, \theta_3] = [10°, 10°, 10°]$

7.1.2 Case 2 Results

In this case, the initial conditions $[\omega_1, \omega_2, \omega_3] = [5, 5, 5] \times 10^{-4}$ rad/s and $[\theta_1, \theta_2, \theta_3] = [10°, 10°, 10°]$ were used. ω_n has also been set to 6 rad/s for this simulation, which corresponds to a settling time of approximately 0.67 s. This is the lowest natural frequency that allows the "actuator dynamics" results to approximately converge for this case.

Angular velocities and Euler angles for this case are shown in Figures 7.6 and 7.7, respectively. While convergence is not as obvious in these plots as it was in the first case, all values trend towards zero. As with the previous case, ω_1 and θ_1 converges more slowly than the other angular velocities and Euler angles. Another set of problematic attitudes can be seen within the first five hours in Figure 7.7, which has the emissive side of the solar sail facing the Sun yet again. Unlike the previous case, the differences shown in Figure 7.8 are much

larger, with the largest angular velocity difference being on the order of 4.5×10^{-4} and the largest Euler angle difference reaching 350°. It is clear that the effect of actuator dynamics has become more significant with an increase in the initial angular velocity.

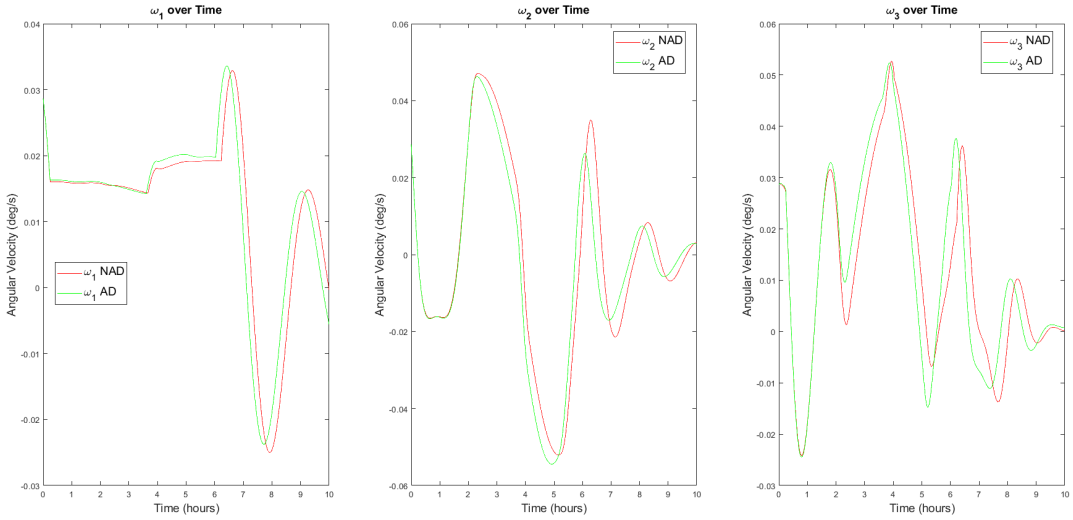

Figure 7.6: Angular Velocities with Setpoint $[\theta_1, \theta_2, \theta_3] = [0°, 0°, 0°]$ and Initial Conditions $[\omega_1, \omega_2, \omega_3] = [5, 5, 5] \times 10^{-4}$ rad/s and $[\theta_1, \theta_2, \theta_3] = [10°, 10°, 10°]$

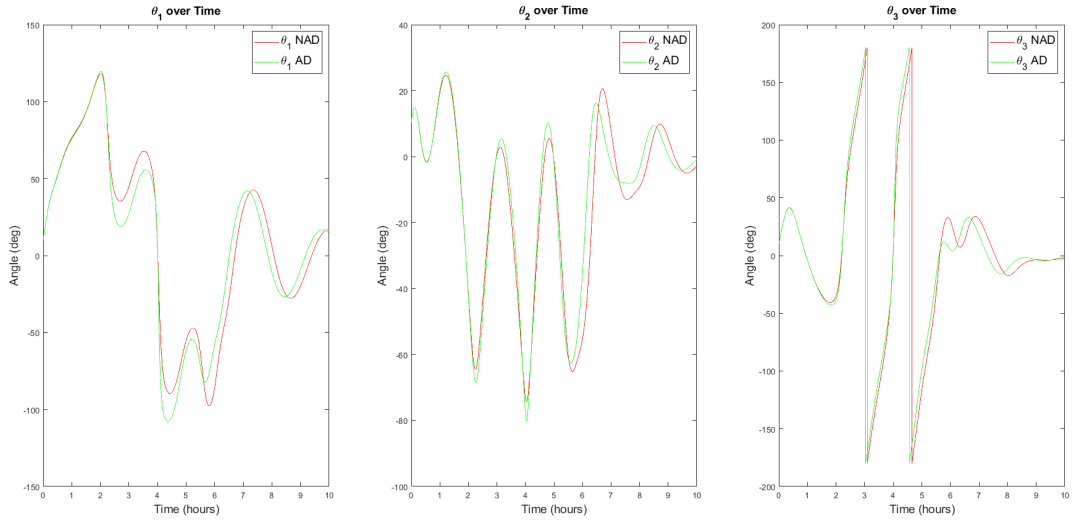

Figure 7.7: Euler Angles with Setpoint $[\theta_1, \theta_2, \theta_3] = [0°, 0°, 0°]$ and Initial Conditions $[\omega_1, \omega_2, \omega_3] = [5, 5, 5] \times 10^{-4}$ rad/s and $[\theta_1, \theta_2, \theta_3] = [10°, 10°, 10°]$

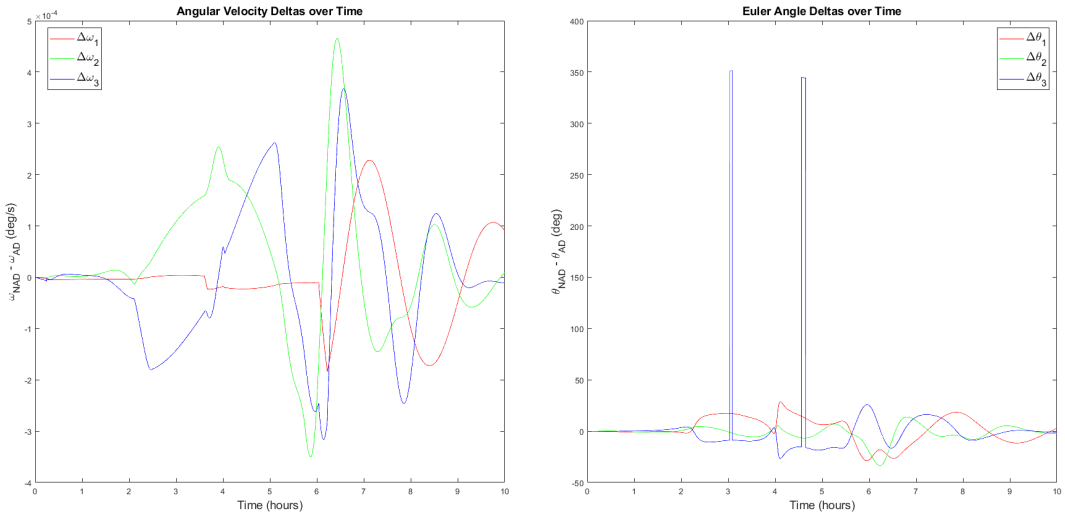

Figure 7.8: Angular Velocity and Euler Angle Deltas with Setpoint $[\theta_1, \theta_2, \theta_3] = [0°, 0°, 0°]$ and Initial Conditions $[\omega_1, \omega_2, \omega_3] = [5, 5, 5] \times 10^{-4}$ rad/s and $[\theta_1, \theta_2, \theta_3] = [10°, 10°, 10°]$

7.2 Zero Initial Angular Velocities and Non-Zero Desired Attitude

In the following two cases, the sail was commanded to the non-zero attitude $[\theta_1, \theta_2, \theta_3] = [20°, 20°, 20°]$ with zero initial angular velocities and varying initial attitudes.

7.2.1 Case 1 Results

In this case, the initial conditions $[\omega_1, \omega_2, \omega_3] = [0, 0, 0]$ rad/s and $[\theta_1, \theta_2, \theta_3] = [10°, 10°, 10°]$ were used.

As shown in Figure 7.9, ω_1 and ω_3 converge more slowly than ω_2, which converges in approximately six hours. As shown in Figure 7.10, the Euler angles are able to converge towards the desired attitude of [20°,20°,20°] after undergoing an initial oscillatory period.

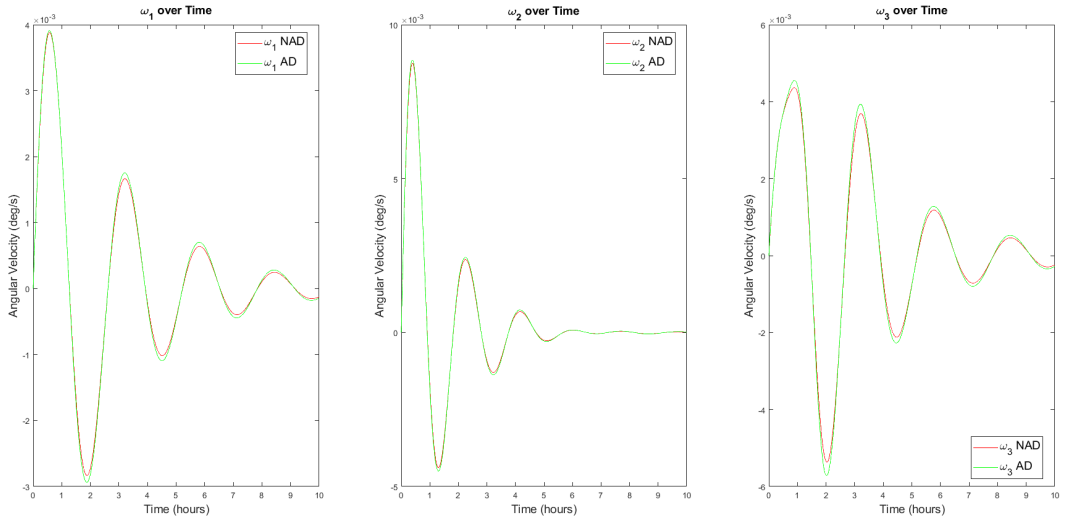

Figure 7.9: Angular Velocities with Setpoint $[\theta_1, \theta_2, \theta_3] = [20°, 20°, 20°]$ and Initial Conditions $[\omega_1, \omega_2, \omega_3] = [0, 0, 0]$ rad/s and $[\theta_1, \theta_2, \theta_3] = [10°, 10°, 10°]$

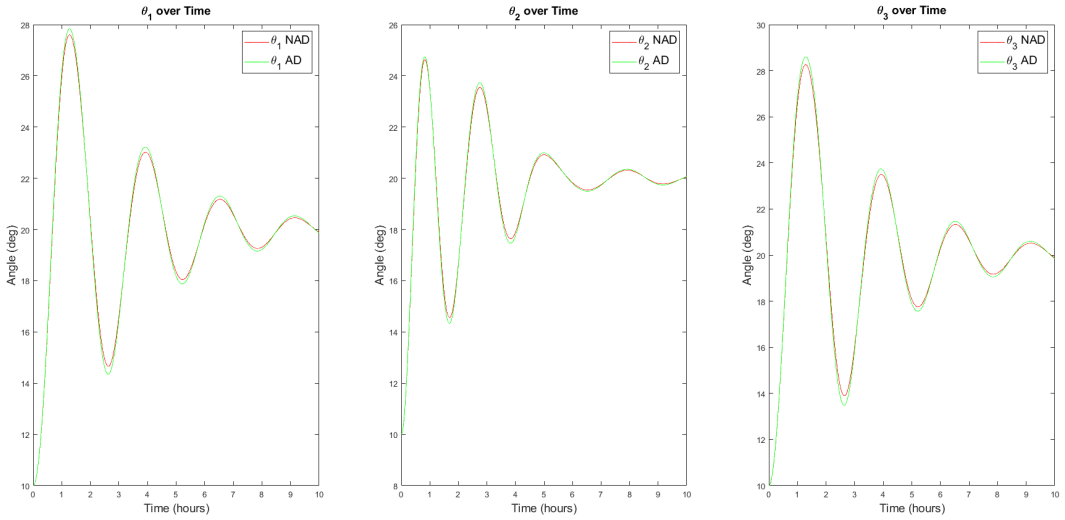

Figure 7.10: Euler Angles with Setpoint $[\theta_1, \theta_2, \theta_3] = [20°, 20°, 20°]$ and Initial Conditions $[\omega_1, \omega_2, \omega_3] = [0, 0, 0]$ rad/s and $[\theta_1, \theta_2, \theta_3] = [10°, 10°, 10°]$

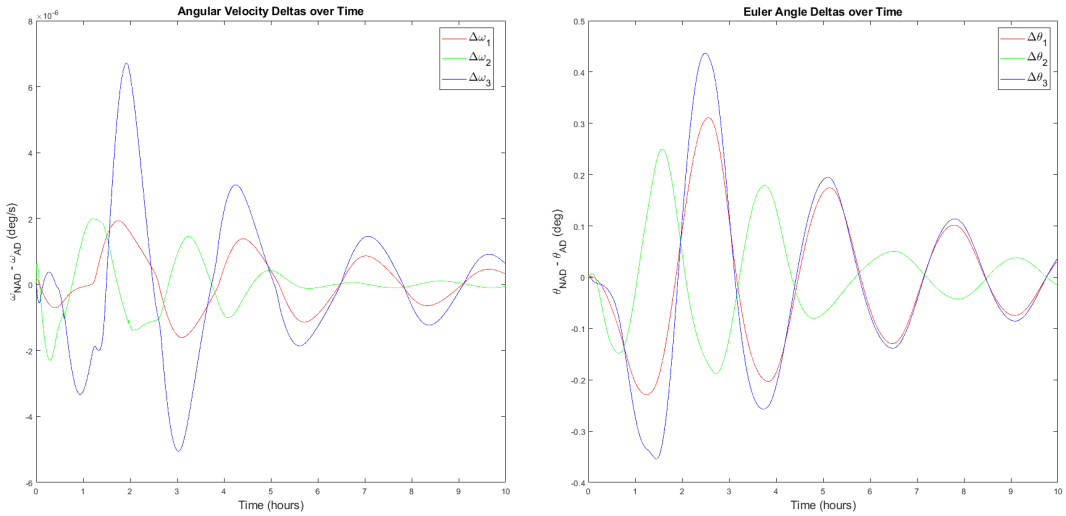

Figure 7.11: Angular Velocity and Euler Angle Deltas with Setpoint $[\theta_1, \theta_2, \theta_3] = [20°, 20°, 20°]$ and Initial Conditions $[\omega_1, \omega_2, \omega_3] = [0, 0, 0]$ rad/s and $[\theta_1, \theta_2, \theta_3] = [10°, 10°, 10°]$

Time histories of the control torques and gimbal and tip vane angles are shown in Figures 7.12 and 7.13, respectively. Over the course of the ten-hour simulation, no significant disparities between the "actuator dynamics" and "no actuator dynamics" results were identified. There are a couple instances where T_{b_2} and T_{b_3} spike within the first two hours, corresponding to rapid changes in the gimbal clock and cone angles.

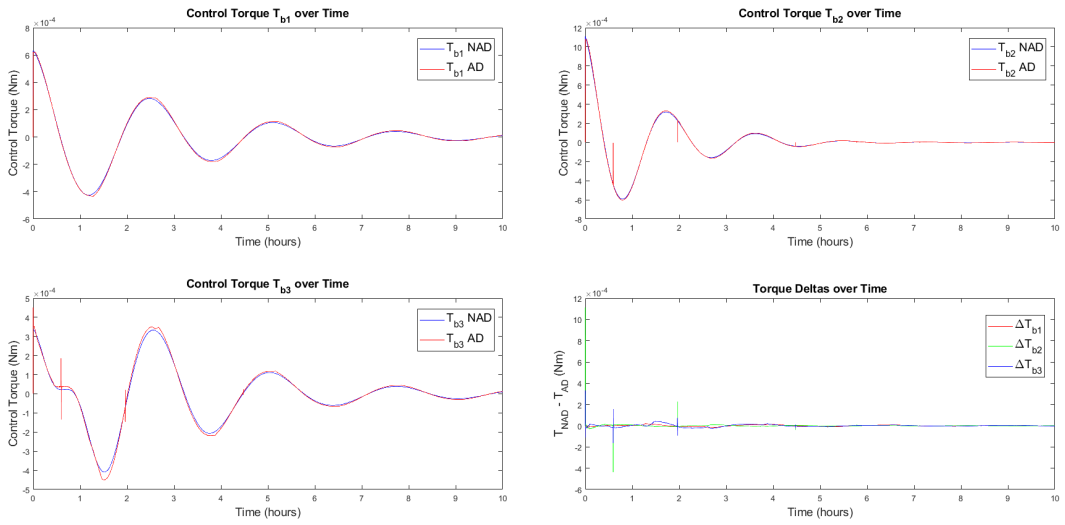

Figure 7.12: Control Torques with Setpoint $[\theta_1, \theta_2, \theta_3] = [20°, 20°, 20°]$ and Initial Conditions $[\omega_1, \omega_2, \omega_3] = [0, 0, 0]$ rad/s and $[\theta_1, \theta_2, \theta_3] = [10°, 10°, 10°]$

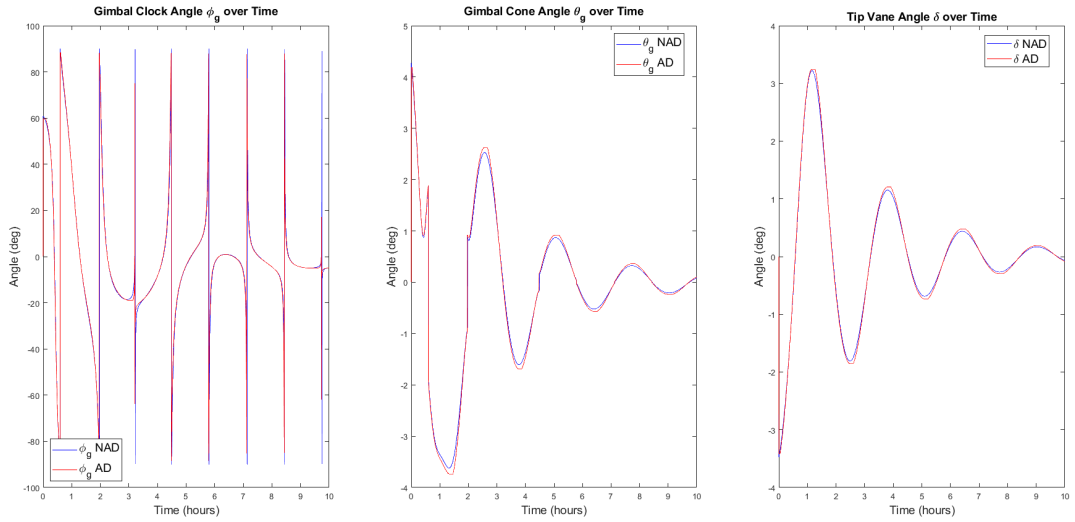

Figure 7.13: Gimbal and Tip Vane Angles with Setpoint $[\theta_1, \theta_2, \theta_3] = [20°, 20°, 20°]$ and Initial Conditions $[\omega_1, \omega_2, \omega_3] = [0, 0, 0]$ rad/s and $[\theta_1, \theta_2, \theta_3] = [10°, 10°, 10°]$

7.2.2 Case 2 Results

In this case, the initial conditions $[\omega_1, \omega_2, \omega_3] = [0, 0, 0]$ rad/s and $[\theta_1, \theta_2, \theta_3] = [30°, 30°, 30°]$ were used.

It can be seen in Figure 7.15 that θ_2 converges faster than in the previous case when

starting at a larger initial value, while θ_1 and θ_3 converge at approximately the same rate as they did in the previous case. Similar to the previous case, Figure 7.16 shows small differences between the "actuator dynamics" and "no actuator dynamics" results that converge towards zero over time.

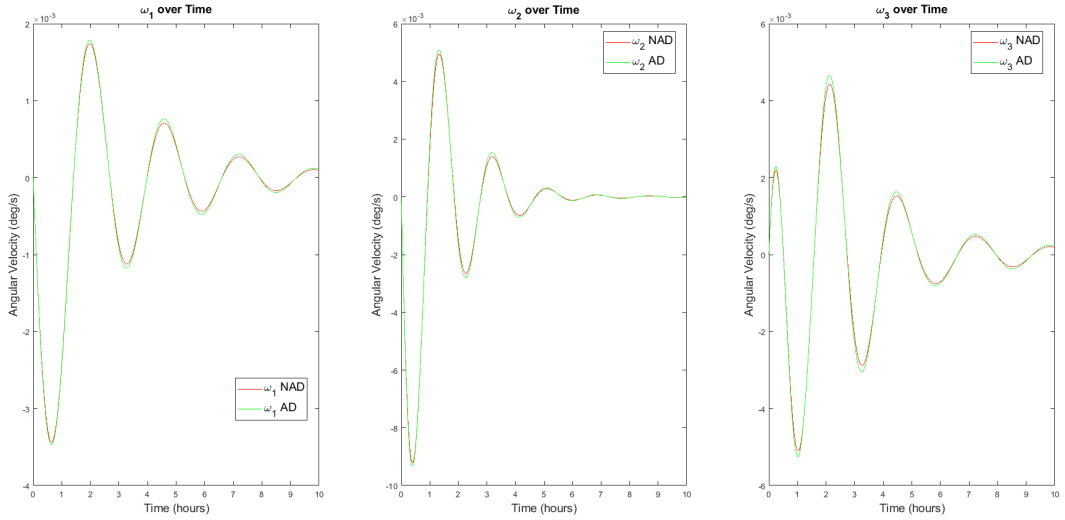

Figure 7.14: Angular Velocities with Setpoint $[\theta_1, \theta_2, \theta_3] = [20°, 20°, 20°]$ and Initial Conditions $[\omega_1, \omega_2, \omega_3] = [0, 0, 0]$ rad/s and $[\theta_1, \theta_2, \theta_3] = [30°, 30°, 30°]$

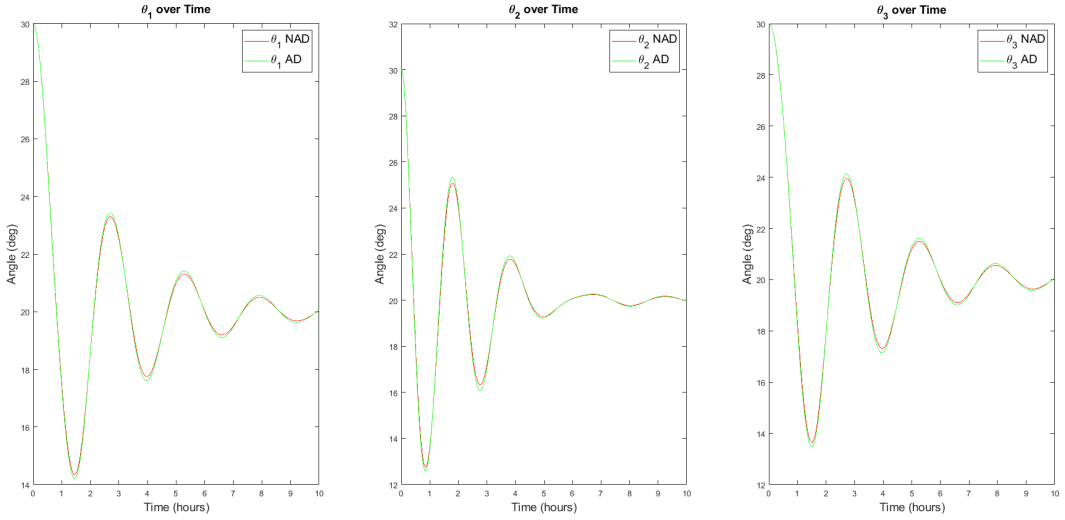

Figure 7.15: Euler Angles with Setpoint $[\theta_1, \theta_2, \theta_3] = [20°, 20°, 20°]$ and Initial Conditions $[\omega_1, \omega_2, \omega_3] = [0, 0, 0]$ rad/s and $[\theta_1, \theta_2, \theta_3] = [10°, 10°, 10°]$

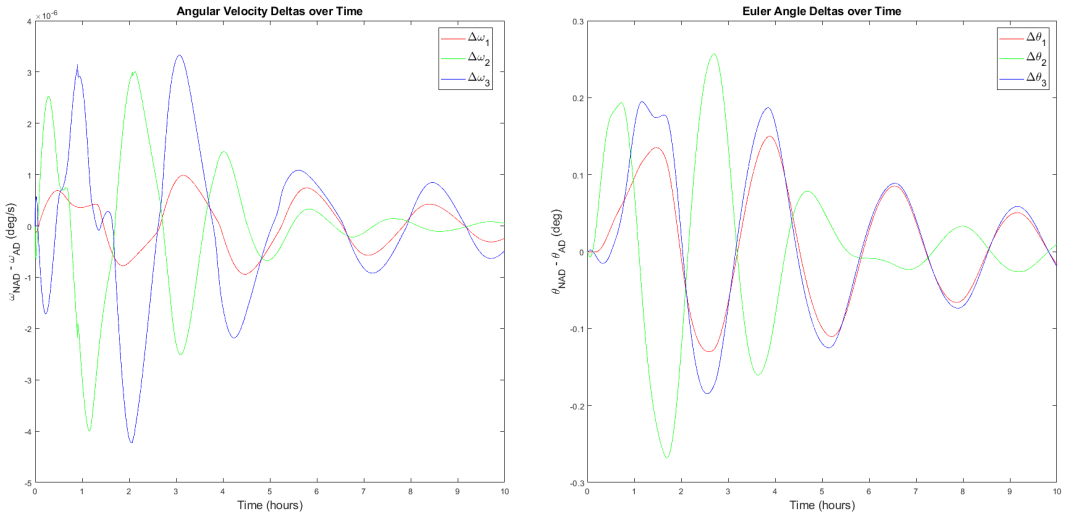

Figure 7.16: Angular Velocity and Euler Angle Deltas with Setpoint $[\theta_1, \theta_2, \theta_3] = [20°, 20°, 20°]$ and Initial Conditions $[\omega_1, \omega_2, \omega_3] = [0, 0, 0]$ rad/s and $[\theta_1, \theta_2, \theta_3] = [10°, 10°, 10°]$

7.3 Summary of Phase 2 Results

The results from this phase have demonstrated that a gimballed mass and two SDOF tip vanes can be used to achieve three-axis control of a solar sail. Both zero and non-zero desired attitudes were simulated, with the control system able to tolerate a range of initial attitudes and angular velocities. It was also observed that the b_2 and b_3 axis torques produced by the tip vanes were not significant enough to disrupt convergence of the system. As was the case with some of the Phase 1 results, a larger motor natural frequency was required for the system to converge for large initial angular velocities and a zero desired attitude. The next phase will further investigate how changes in the motor natural frequency influence the results.

8 Phase 3 Simulation Results

The focus of Phase 3 was to assess the sensitivity of the system to changes in some of the input parameters. The parameters of interest for these studies were the natural frequency of the motors, ω_n, the gimballed payload mass, m_p, and the tip vane surface area, A_{tv}. Actuator dynamics were taken into account for all of these studies. The Phase 3 simulation results are examined in the following sections.

8.1 Variation in Motor Natural Frequency

For this study, the sail was commanded to a zero attitude with varying initial angular velocities and a constant initial attitude of $[\theta_1, \theta_2, \theta_3] = [10°, 10°, 10°]$ and initial angular velocities of $[\omega_1, \omega_2, \omega_3] = [5, 5, 5] \times 10^{-4}$ rad/s.

As can be seen in 8.1, an increase in the motor natural frequency results in faster convergence. For this particular set of initial conditions, there exists a threshold between $\omega_n = 5$ to $\omega_n = 7$ rad/s, above which the results begin to converge. Beyond $\omega_n = 7$, there is little variation in the angular velocities and Euler angles. It can also be seen that regardless of the natural frequency, all plots mostly overlap within the first four hours, after which they begin to diverge from each other.

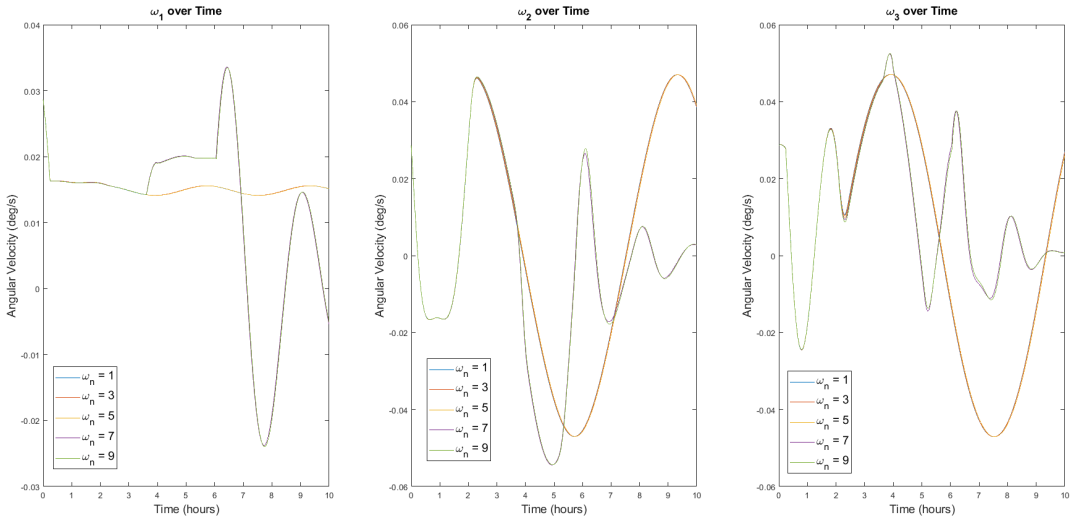

Figure 8.1: Variation in Angular Velocities with $\omega_n = [1, 3, 5, 7, 9]$ rad/s, Setpoint $[\theta_1, \theta_2, \theta_3] = [0°, 0°, 0°]$, and Initial Conditions $[\omega_1, \omega_2, \omega_3] = [5, 5, 5] \times 10^{-4}$ rad/s and $[\theta_1, \theta_2, \theta_3] = [10°, 10°, 10°]$

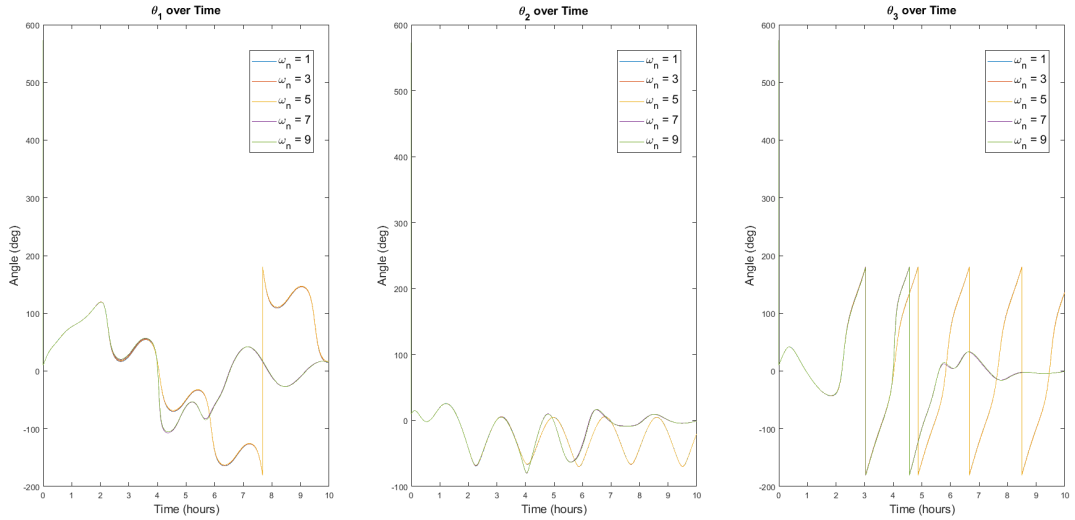

Figure 8.2: Variation in Euler Angles with $\omega_n = [1, 3, 5, 7, 9]$ rad/s, Setpoint $[\theta_1, \theta_2, \theta_3] = [0°, 0°, 0°]$, and Initial Conditions $[\omega_1, \omega_2, \omega_3] = [5, 5, 5] \times 10^{-4}$ rad/s and $[\theta_1, \theta_2, \theta_3] = [10°, 10°, 10°]$

8.2 Variation in Gimballed Payload Mass and Tip Vane Surface Area

For this study, the two parameters that have the most significant impact on the control torques produced, the gimballed payload mass and the tip vane surface area, are varied to understand their impact on the system response. The setpoint and initial conditions are the same as in Section 8.1, except the initial angular velocities have been lowered to $[\omega_1, \omega_2, \omega_3] = [5, 5, 5] \times 10^{-5}$ rad/s.

For the first case, the derivative gain, K_d, was set to 200 Nm/rad/s and the proportional gain, K_p, was set to 1 Nm. This was done to minimize overshoot, and reduce the rise and settling times. The gimballed payload mass and tip vane surface areas remain unchanged from the previous sections and all the motor angular velocities have been set to 1 rad/s.

The results in Figure 8.3 show that all the angular velocities and Euler angles are able to converge within one hour except for ω_1 and θ_1, which are unable to converge. This means that the current tip vane surface area is insufficient and must be increased to be able to generate the necessary control torques.

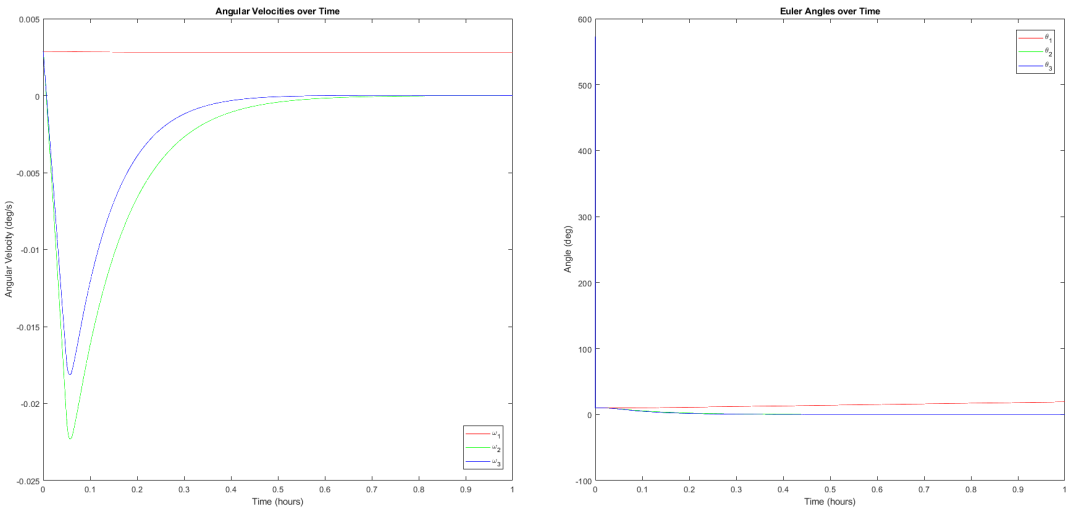

Figure 8.3: Angular Velocities and Euler Angles with $m_p = 116$ kg, $A_{tv} = 20\text{m}^2$, Setpoint $[\theta_1, \theta_2, \theta_3] = [0°, 0°, 0°]$, and Initial Conditions $[\omega_1, \omega_2, \omega_3] = [5, 5, 5] \times 10^{-5}$ rad/s and $[\theta_1, \theta_2, \theta_3] = [10°, 10°, 10°]$

In an effort to make all of the results converge, the tip vane surface area was increased to 200m^2. The gimballed mass payload was also increased to 500 kg to see if that would influence the convergence of the other results. As shown in 8.4, if these parameters increase, then all the angular velocities and Euler angles converge within one hour. The rise times for ω_2 and ω_3 have also increased slightly compared to the previous case, however, they still converge within one hour like before.

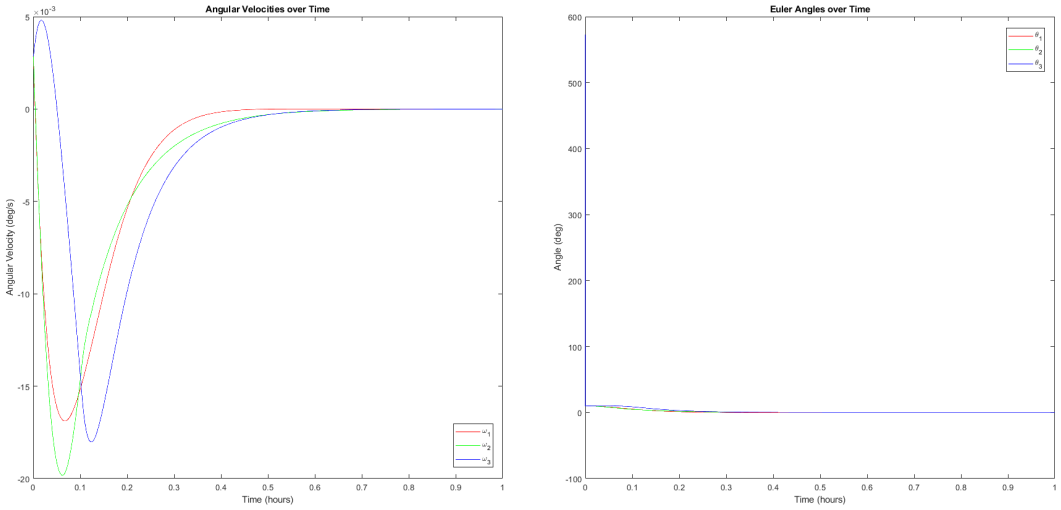

Figure 8.4: Angular Velocities and Euler Angles with $m_p = 500$ kg, $A_{tv} = 200\text{m}^2$, Setpoint $[\theta_1, \theta_2, \theta_3] = [0°, 0°, 0°]$, and Initial Conditions $[\omega_1, \omega_2, \omega_3] = [5, 5, 5] \times 10^{-5}$ rad/s and $[\theta_1, \theta_2, \theta_3] = [10°, 10°, 10°]$

8.3 Summary of Phase 3 Results

This results from this section have demonstrated the sensitivity of the system to changes in the motor natural frequencies, as well as the gimballed payload mass and tip vane surface area. For higher initial angular velocities, motors with shorter settling times are needed to ensure the results converge. To produce larger control torques, it was shown that a larger tip vane surface area was needed, however an increase in the gimballed payload mass did not appear to significantly alter the results between the two cases that were analyzed. Additional simulations were performed that incorporated a lower gimballed payload mass and the same

initial conditions, and it was discovered that a gimballed mass as low as 10 kg was still able to achieve convergence within one hour.

One tradeoff of producing larger torques is that the actuator size must also increase. In this case, the tip vane surface area needed to be increased by a factor of ten, adding 1.56 kg of sail film, based on the film density from Table 5.1. This may seem insignificant compared to the overall spacecraft mass, however given the significant increase in tip vane surface area, it is likely that larger supporting structures would be needed to ensure the tip vane film remained adequately tensioned. Any type of spacecraft mass increase would be undesirable since that would limit the sail's maximum possible acceleration.

9 Conclusions and Future Work

9.1 Conclusions

This thesis has demonstrated the viability of a combined gimballed mass and two SDOF tip vane control system and has investigated its limitations.

In Section 5, a dynamic model of a rigid sqaure solar sail spacecraft was developed. The necessary equations for the gimbal and tip vane angles were derived and a control scheme that incorporated second-order actuator dynamics was implemented.

In Section 6, a solar sail equipped with only a gimballed mass actuator was simulated to demonstrate control authority over the b_2 and b_3 axes. The results indicated that the system performed well for low initial angular velocities and a zero attitude setpoint, but had difficulty converging when they were increased to 5×10^{-4} rad/s. It was later discovered that increasing the natural frequency of the gimbal motors was necessary for the system to converge in this case. The system did not encounter any issues converging to a non-zero setpoint with all-zero initial angular velocities.

In Section 7, two SDOF tip vane actuators were added to the control system to achieve three-axis control of the solar sail. Similarly to the sail with just a gimballed mass, it could only regulate large initial angular velocities if the gimbal and tip vane motor natural frequencies were increased. Non-zero attitude setpoints were also achieved with theis system.

In Section 8, the motor natural frequencies, gimballed payload mass, and tip vane surface area were varied to better understand the sensitivity of the system. It was discovered that an increase in the motor natural frequency results in a faster response for higher initial angular velocities. To achieve a faster system response, it was necessary to increase the control gains, which necessitated a larger tip vane surface area than what was used in the prior sections. Increasing the gimballed payload mass did not significantly alter the ω_2, ω_3, θ_2, and θ_3 results in this case, demonstrating the versatility of the gimballed mass actuator for low initial angular velocities. However, there may be other cases where a larger gimballed

payload mass could have a greater impact on the system response, and therefore, variation of this parameter warrants further investigation.

Ultimately, this work serves as a foundation for future studies in the field to expand upon. Future investigations could build higher fidelity models to gain a better understanding of the system's limitations. Potential areas of investigation are discussed next.

9.2 Future Work

9.2.1 Improvements to the Control System

This control system could be further augmented by building in a recovery state for the sail whenever the emissive side is facing the Sun. The results from Sections 6 and 7 have demonstrated that this attitude can be encountered for large initial angular velocities. Convergence takes much longer in these cases and has the emissive side facing the Sun a few times, which complicates temperature regulation. To address this problem, the tip vanes could be programmed to have their reflective sides face the Sun and produce recovery torques, potentially restoring the sail to its desired attitude faster than it otherwise would have taken.

9.2.2 Sail Flexibility

The simulations performed as part of this research incorporated irregularities in the sail membrane, such as membrane wrinkling and billowing, in the form of the sail thrust coefficient. To accurately capture the behaviour of the sail membrane when subjected to SRP loading, the sail should be modeled as a flexible body. To accomplish this, a finite element model should be developed and integrated into the existing simulation similar to the one developed by Choi for a cord mat square solar sail [32].

9.2.3 Realistic SRP Force

As discussed in Section 2, the SRP force model used for this research was an idealized form that considered all incident solar radiation to be specularly reflected. This may be sufficient

for preliminary mission analyses, but for higher fidelity studies, the other contributions to the SRP force from diffuse reflection, absorption, and emission of light should also be incorporated into the simulation. These effects would result in both normal and tangential components of the SRP force [15], which could result in additional torques that are difficult to control.

References

[1] R. L. Garwin. "Solar Sailing: A Practical Method of Propulsion within the Solar System". In: *Jet Propulsion* 28.123 (Mar. 1958), pp. 188–190.

[2] L. Friedman et al. "Solar Sailing - The concept made realistic". In: *16th Aerospace Sciences Meeting*. Jan. 1978. DOI: 10.2514/6.1978-82.

[3] L. Johnson, R. M. Young, and E. E. Montgomery IV. "Recent advances in solar sail propulsion systems at NASA". In: *Acta Astronautica* 61.1-6 (June 2007), pp. 376–382. DOI: 10.1016/j.actaastro.2007.01.047.

[4] G. Vulpetti, L. Johnson, and G. L. Matloff. *Solar Sails: A Novel Approach to Interplanetary Travel*. 2nd ed. Springer, 2015.

[5] Y. Tsuda et al. "Achievement of IKAROS - Japanese deep space solar sail demonstration mission". In: *Acta Astronautica* 82.2 (Feb. 2013), pp. 183–188. DOI: 10.1016/j.actaastro.2012.03.032.

[6] *The Story of LightSail, Part 2*. eoPortal. URL: https://www.planetary.org/sci-tech/the-story-of-lightsail-part-2.

[7] *LightSail*. eoPortal. URL: https://www.eoportal.org/satellite-missions/lightsail.

[8] *LightSail-2*. eoPortal. URL: https://www.eoportal.org/satellite-missions/lightsail-2.

[9] *NASA Solar Sail Mission to Chase Tiny Asteroid After Artemis I Launch*. JPL. URL: https://www.jpl.nasa.gov/news/nasa-solar-sail-mission-to-chase-tiny-asteroid-after-artemis-i-launch.

[10] *NEA Scout Status Update*. NASA. URL: https://www.nasa.gov/centers/marshall/news/2022/nea-scout-status-update.html.

[11] M. Macdonald et al. "Solar Polar Orbiter: A Solar Sail Technology Reference Study". In: *Journal of Spacecraft and Rockets* 43.5 (Sept. 2006), pp. 960–972. DOI: 10.2514/1.16408.

[12] A. Lyngvi, P. Falkner, and A. Peacock. "The interstellar heliopause probe technology reference study". In: *Advances in Space Research* 35.12 (Jan. 2005), pp. 2073–2077. DOI: 10.1016/j.asr.2005.07.083.

[13] D. A. Spencer et al. "The LightSail 2 solar sailing technology demonstration". In: *Advances in Space Research* 67.9 (May 2021), pp. 2878–2889. DOI: 10.1016/j.asr.2020.06.029.

[14] *NEA Scout*. eoPortal. URL: https://www.eoportal.org/satellite-missions/nea-scout.

[15] B. Fu, E. Sperber, and F. Eke. "Solar sail technology—A state of the art review". In: *Progress in Aerospace Sciences* 86 (Oct. 2016), pp. 1–19. DOI: 10.1016/j.paerosci.2016.07.001.

[16] C. R. McInnes. *Solar Sailing: Technology, Dynamics and Mission Applications*. 1st ed. Springer, 2004.

[17] B. Wie. "Solar Sail Attitude Control and Dynamics, Part 1". In: *Journal of Guidance, Control, and Dynamics* 27.4 (July 2004), pp. 526–535. DOI: 10.1016/j.paerosci.2016.07.001.

[18] E. Sperber. "Attitude Dynamics and Control of Solar Sails". PhD Dissertation. University of California, Davis, 2014.

[19] R. H. MacNeal, J. M. Hedgepeth, and H. U. Schuerech. *Heliogyro Solar Sailer: Summary Report*. Contractor Report. NASA, June 1969. URL: https://ntrs.nasa.gov/citations/19690019483.

[20] R. L. Sohn. "Attitude Stabilization by Means of Solar Radiation Pressure". In: *ARS Journal* 29 (May 1959), pp. 371–373.

[21] F. Angrilli and S. Bortolami. "Attitude and Orbital Modeling of Solar-Sail Spacecraft". In: *ESA Journal* 14.4 (Jan. 1990), pp. 431–446.

[22] E. Sperber, B. Fu, and F. O. Eke. "Large Angle Reorientation of a Solar Sail Using Gimballed Mass Control". In: *J of Astronaut Sci* 63 (June 2016), pp. 103–123. DOI: 10.1007/s40295-016-0085-1.

[23] B. Wie. "Solar Sail Attitude Control and Dynamics, Part 2". In: *Journal of Guidance, Control, and Dynamics* 27.4 (July 2004), pp. 536–544. DOI: 10.2514/1.11133.

[24] J. Liu et al. "Dynamics and Control of a Flexible Solar Sail". In: *Mathematical Problems in Engineering* 2014 (Nov. 2014). DOI: 10.1155/2014/868419.

[25] L. Wu et al. "Modeling and attitude control for solar sail based on gimbal boom". In: *2015 5th Australian Control Conference (AUCC)*. Nov. 2015, pp. 283–287.

[26] B. Wie and D. Murphy. "Solar-Sail Attitude Control Design for a Flight Validation Mission". In: *Journal of Spacecraft and Rockets* 44.4 (July 2007), pp. 809–821. DOI: 10.2514/1.22996.

[27] S. N. Adeli, V. J. Lappas, and B. Wie. "A scalable bus-based attitude control system for Solar Sails". In: *Advances in Space Research* 48.11 (Dec. 2011), pp. 1836–1847. DOI: 10.1016/j.asr.2011.08.024.

[28] M. Choi and C. J. Damaren. "Structural Dynamics and Attitude Control of a Solar Sail Using Tip Vanes". In: *Journal of Spacecraft and Rockets* 52.6 (Nov. 2015), pp. 1665–1679. DOI: 10.2514/1.A33179.

[29] J. J. Bladt and D. A. Lawrence. "Solar sail attitude control performance comparison". In: *AAS Guidance and Control Conference*. Jan. 2005. URL: https://ntrs.nasa.gov/citations/20050137595.

[30] M. Leipold et al. "ODISSEE — A proposal for demonstration of a solar sail in earth orbit". In: *Acta Astronautica* 45.4–9 (Aug. 1999), pp. 557–566. DOI: 10.1016/S0094-5765(99)00176-9.

[31] K. Ogata. *Modern Control Engineering*. 5th ed. Prentice Hall, 2010.

[32] M. Choi. "Flexible Dynamics and Attitude Control of a Square Solar Sail". PhD Dissertation. University of Toronto, 2015.